Journal of Geophysical Research: Space Physics

RESEARCH ARTICLE
10.1029/2018JA025932

Planetary Period Modulation of Reconnection Bursts in Saturn's Magnetotail

T. J. Bradley[1], **S. W. H. Cowley**[1], **E. J. Bunce**[1], **A. W. Smith**[2], **C. M. Jackman**[2], **and G. Provan**[1]

[1]Department of Physics and Astronomy, University of Leicester, Leicester, UK, [2]Department of Physics and Astronomy, University of Southampton, Southampton, UK

Key Points:
- We analyze a catalogue of 2,094 reconnection events in Saturn's magnetotail and organize them according to northern and southern PPO phases
- Events are best organized by local PPO phases rather than global phases, implying that reconnection is more locally than globally triggered
- Events are best organized by phases where the tail current sheet should be locally thin and the field lines near maximum radial displacement

Correspondence to:
T. J. Bradley,
tb252@le.ac.uk

Citation:
Bradley, T. J., Cowley, S. W. H., Bunce, E. J., Smith, A. W., Jackman, C. M., & Provan, G. (2018). Planetary period modulation of reconnection bursts in Saturn's magnetotail. *Journal of Geophysical Research: Space Physics*, *123*, 9476–9507. https://doi.org/10.1029/2018JA025932

Received 23 JUL 2018
Accepted 1 NOV 2018
Accepted article online 6 NOV 2018
Published online 28 NOV 2018

Abstract We conduct a statistical analysis of 2,094 reconnection events in Saturn's near-equatorial magnetotail previously identified in Cassini magnetometer data from intervals during 2006 and 2009/2010. These consist of tailward propagating plasmoids and planetward propagating dipolarizations, with approximately twice as many plasmoids as dipolarizations. We organize these by three related planetary period oscillation (PPO) phase systems, the northern and southern PPO phases relative to noon, the same phases retarded by a radial propagation delay, and the local retarded phases that take account of the azimuth (local time) of the observation. Clear PPO modulation is found for both plasmoid and dipolarization events, with local retarded phases best organizing the event data with the modulation in event frequency propagating across the tail as the PPO systems rotate. This indicates that the events are localized in azimuth, rather than simultaneously affecting much of the tail width. Overall, events occur preferentially by factors of ~3 at northern and southern phases where the tail current sheet is expected locally to be thinnest in the PPO cycle, with field lines contracting back from their maximum radial displacement, compared with the antiphase conditions. Separating the events into those representing the start of independent reconnection episodes, occurring at least 3 hr after the last, and events in subsequent clusters, shows that the above phases are predominantly characteristic of the majority cluster events. The phases at the start of independent reconnection episodes are typically ~60° earlier.

1. Introduction

The large-scale dynamics of Saturn's magnetosphere are related to the action and interplay of three main processes. The first is the injection of water plasma into the near-corotating inner magnetosphere from the moon Enceladus, and its subsequent outward transport and downtail loss as plasmoids via reconnection in the nightside plasma sheet, forming the Vasyliunas cycle (e.g., Chen et al., 2010; Cowley et al., 2004, 2015, Hill et al., 2008; Jackman et al., 2007, 2015; Liu et al., 2010; Liu & Hill, 2012; Pontius & Hill, 2009; Vasyliunas, 1983). The second is the magnetospheric interaction with the interplanetary medium at the dayside magnetopause, which results in the transport of open flux into the tail and its closure and return also via reconnection in the plasma sheet, forming the Dungey cycle (e.g., Badman et al., 2005, 2013; Badman & Cowley, 2007; Cowley et al., 2005; Dungey, 1961; Jackman et al., 2011; Radioti et al., 2011, 2013; Thomsen et al., 2015). The third is the modulation near the planetary rotation period (~10.7 hr) driven from the northern and southern polar ionospheres forming the *planetary period oscillations* (PPOs), which are ubiquitous in plasma-related parameters throughout Saturn's magnetosphere (e.g., Carbary & Mitchell, 2013; Espinosa et al., 2003; Gurnett et al., 2009; Jia et al., 2012; Provan et al., 2016). Principal data sets relevant to the study of the dynamics to which these processes give rise include ultraviolet (UV) auroral imagery obtained both by the Cassini spacecraft and by the Hubble Space Telescope, which display the structure and evolution of precipitating energetic magnetospheric plasma particles (e.g., Clarke et al., 2005, 2009; Grodent et al., 2011; Nichols et al., 2014), observations of related auroral radio emissions generated in the kilometer wave band by accelerated auroral electrons that can be monitored near-continuously, termed Saturn kilometric radiation (SKR; e.g., Kurth et al., 2005; Lamy et al., 2010, 2013), and energetic neutral atom (ENA) images that can track the evolution of hot plasma populations in the magnetosphere as the energetic ions charge exchange with orbiting neutral gas (e.g., Krimigis et al., 2007; Mitchell et al., 2005, 2009).

Also relevant are observations of reconnection-related phenomena in the magnetic field and plasma in Saturn's magnetotail. Specifically, reconnection within the near-planet plasma sheet pinches off sections of

the sheet, which then propagate tailward as closed field loop plasmoids (Hill et al., 2008; Jackman et al., 2007, 2008, 2011) while also generating a field dipolarization on the other side of the reconnection site, which propagates planetward, accelerating the plasma as it does so (Bunce et al., 2005; Jackman et al., 2013, 2015; Smith, Jackman, Thomsen, Lamy, & Sergis, 2018; Smith, Jackman, Thomsen, Sergis, et al., 2018; Thomsen et al., 2013, 2015). These reconnection-related phenomena are most readily recognized through perturbations in the near-equatorial colatitudinal magnetic field component (positive southward), which, given the sense of Saturn's internal planetary field (positive at the equator), produces positive to negative deflections for tailward propagating plasmoids and negative to positive deflections for planetward propagating dipolarizations, with durations typically of ~5–10 min (e.g., Jackman et al., 2014; Smith et al., 2016).

Studies of auroral UV and radio data during the Cassini mission have shown that dynamic phenomena within Saturn's magnetosphere can broadly be divided into two categories. The first takes place on timescales related to Saturn's rotation period, more specifically to the rotation period of the PPOs. These dynamic events are associated with recurrent few-hour intensifications in the power of SKR emissions, together with extensions of the spectrum to lower frequencies (e.g., Jackman et al., 2009; Lamy et al., 2013; Reed et al., 2018). The extension of the spectrum is indicative of the enhancement of field-aligned magnetosphere-ionosphere coupling current densities with consequent electron acceleration extending to higher altitudes and lower field strengths along auroral field lines (e.g., Cowley & Bunce, 2003). This inference follows from the fact that SKR is emitted from its source region at a frequency close to the local electron gyrofrequency (e.g., Lamy et al., 2010). Related UV auroral features include the formation of bright patches and structured arcs typically in the midnight-to-dawn sector, followed by propagation of these enhancements via dawn into the dayside sector over the same few-hour interval as the SKR power enhancement (Jackman et al., 2013; Mitchell et al., 2009; Radioti et al., 2016). Concurrent ENA images show that these events are associated with the injection of hot plasma into the outer nightside magnetosphere from the tail, followed by subcorotating propagation via dawn to the dayside, and beyond, in concert with the auroral UV enhancement and propagation (Mitchell et al., 2005, 2009). Taken together, these properties are strongly indicative of the occurrence of bursts of reconnection in the tail, likely principally associated with the Vasyliunas cycle given that the amount of open flux in the system, contained poleward of the auroral region, does not change significantly during these events (Radioti et al., 2016). We note, however, that although such events tend to be recurrent at the PPO rotation period, as indicated above, it is not the case that they occur on every PPO rotation cycle (Mitchell et al., 2009; Reed et al., 2018).

The second category of dynamic event also exhibits elevated SKR powers with low-frequency spectrum extensions, auroral enhancements, which propagate from nightside to dayside via dawn, and nightside plasma injections indicative of tail reconnection bursts. Now, however, the events typically last for intervals of several planetary rotation (or PPO) periods, and the enhanced dawn auroras expand in width significantly poleward, sometimes to the planetary pole itself, indicative of the closure of significant amounts of open tail flux as part of the Dungey cycle (Badman et al., 2005; Clarke et al., 2005; Cowley et al., 2005; Grodent et al., 2005; Meredith et al., 2014; Mitchell et al., 2009; Nichols et al., 2014). Related in situ Cassini observations of hot plasma and unusually intense structured field-aligned currents extending to near the pole in the midnight-to-dawn sector have also been reported (Bunce et al., 2010). As initially discerned from Voyager upstream solar wind and SKR power data (Desch, 1982; Desch & Rucker, 1983), such events are associated with strong magnetospheric compressions by the solar wind, due either to the effect of semi-recurrent corotating interaction regions (CIRs) or to coronal mass ejections (CMEs; Badman et al., 2016; Bunce et al., 2006; Clarke et al., 2005; Prangé et al., 2004). They thus take place on timescales of some fraction of an ~25-day equatorial solar rotation period, typically every ~1–3 weeks, and last typically for 1–3 days, though then perhaps consisting of more than one enhancement during the interval of solar wind disturbance (Meredith et al., 2014; Reed et al., 2018). On the latter point, we note that the SKR emissions may continue to be modulated near the PPO period throughout such extended events (Badman et al., 2008).

Given these findings, it is evident that observations of reconnection-related phenomena in Saturn's magnetotail, specifically of tailward propagating plasmoids and planetward propagating dipolarizations, are of direct relevance to discussion of Saturn's magnetospheric dynamics. Following the initial studies cited above, a catalogue of 99 tail events was presented by Jackman et al. (2014), observed during the 2006 sequence of nightside Cassini orbits in the midnight to dawn sector and selected using simple magnitude criteria for the north-south field deflections. Subsequently, the search was automated by Smith et al.

(2016) and expanded to include nightside data from 2009/2010 obtained in the dusk to midnight sector. This study yielded a total of 2,094 tail events spanning from dusk to near dawn, consisting of 1,382 tailward propagating plasmoids and 712 planetward propagating dipolarizations, together constituting 220 isolated reconnection events and 381 event clusters with members separated by less than 3 hr. Some of these events must have been associated with solar wind compressions, as exemplified by one dipolarization, which occurred during the Cassini Saturn orbit insertion pass in 2004 (Bunce et al., 2005; Jackman et al., 2005). However, the overall frequency of the events, isolated plus clusters, approaching a peak rate of one per ~10.7-hr PPO period during intervals when the spacecraft was located in the tail close to the plasma sheet (Smith et al., 2016) makes it clear that, in general, they are more likely associated with recurrent events associated with the PPO cycle. In an investigation of an initial set of nine such events, Jackman et al. (2009) showed that eight were associated with SKR bursts, starting on the rising phase of the PPO-related SKR modulation cycle.

Studies of Saturn's magnetotail have shown that the field and plasma are significantly modulated by the PPOs in such a way that its stability to reconnection may be affected, with the northern and southern tail lobes being dominated by the PPO signals from the two corresponding polar ionospheres, while the plasma sheet region between is dual modulated by both (Provan et al., 2012). Initially, it was shown that the plasma sheet undergoes north-south oscillations during the PPO cycle (Arridge et al., 2011; Carbary et al., 2008), with maximum effect occurring when the northern and southern PPO systems are combined in phase (see section 2.3 for further details; Provan et al., 2012; Szego et al., 2013). It was further shown, however, that the PPOs also modulate the thickness of the plasma sheet (Morooka et al., 2009), with maximum effect when the two systems are combined in antiphase (Provan et al., 2012). These modulations give rise to a range of distinctive behaviors of the tail field depending on the relative amplitudes and phases of the northern and southern PPO perturbations, including sawtooth-like oscillations of the radial field when the northern and southern PPOs are of comparable strength and combined near to quadrature (Cowley et al., 2017; Cowley & Provan, 2017; Thomsen et al., 2017). Clearly, such modulations may affect the stability of the plasma/current sheet, with reconnection being more likely to occur, for example, when the sheet is thin and the current most intense. In addition, it has been found that the equatorial magnetospheric plasma also undergoes radial displacements during the PPO cycle that are in quadrature with both the north-south displacements and the thickness modulations, as detected directly in motions of the dayside magnetopause and bow shock (Clarke, Andrews, Arridge, et al., 2010; Clarke, Andrews, Coates, et al., 2010), and in latitude displacements of field-aligned current systems in the auroral regions (Hunt et al., 2014). Again, we may expect reconnection to be favored and plasmoid formation to be enhanced when the plasma mass is displaced outward rather than when it is displaced inward. In an initial study of the PPO-dependency of reconnection-related events in the tail, Jackman et al. (2016) employed the catalogue of plasmoid events presented by Jackman et al. (2014), consisting of 65 isolated events or clusters. They showed that their occurrence is indeed significantly modulated by the PPOs, with events occurring preferentially at phases where the plasma is displaced radially outward and the sheet thinned, as anticipated.

Such reconnection events occurring within a given longitude sector will generate a magnetosphere-ionosphere *current wedge* configuration on the nightside, first described for Earth during substorms by McPherron et al. (1973). Hot plasma is injected into the outer magnetosphere from the tail within the wedge, with auroral enhancements being due both to precipitation of the hot plasma and to regions of intense upward directed field-aligned current associated with the wedge (Cowley et al., 2005; Jackman et al., 2013). At Saturn such reconnection-related events will be followed by rotational transport of the hot injected plasma and associated wedge current system into the dawn and dayside sector, as observed during recurrent dynamic events (Mitchell et al., 2009). This picture thus potentially provides a coherent framework within which to understand the triggering of such events during the PPO cycle, with *missing* events corresponding to PPO cycles on which conditions were such that reconnection was not triggered, due either to unfavorable plasma or field conditions in the subcorotating magnetodisk or to weak amplitudes and unfavorable relative phases of the two PPO systems. However, the previous studies of the PPO dependence of reconnection-related events in Saturn's tail by Jackman et al. (2009, 2013) were based on a limited set of events, while the much expanded catalogue presented by Smith et al. (2016) provides the opportunity to explore these relations in significantly greater detail, over a greater range of nightside local times (LTs), and not only for plasmoids but also for dipolarization events. These are the topics of the present paper.

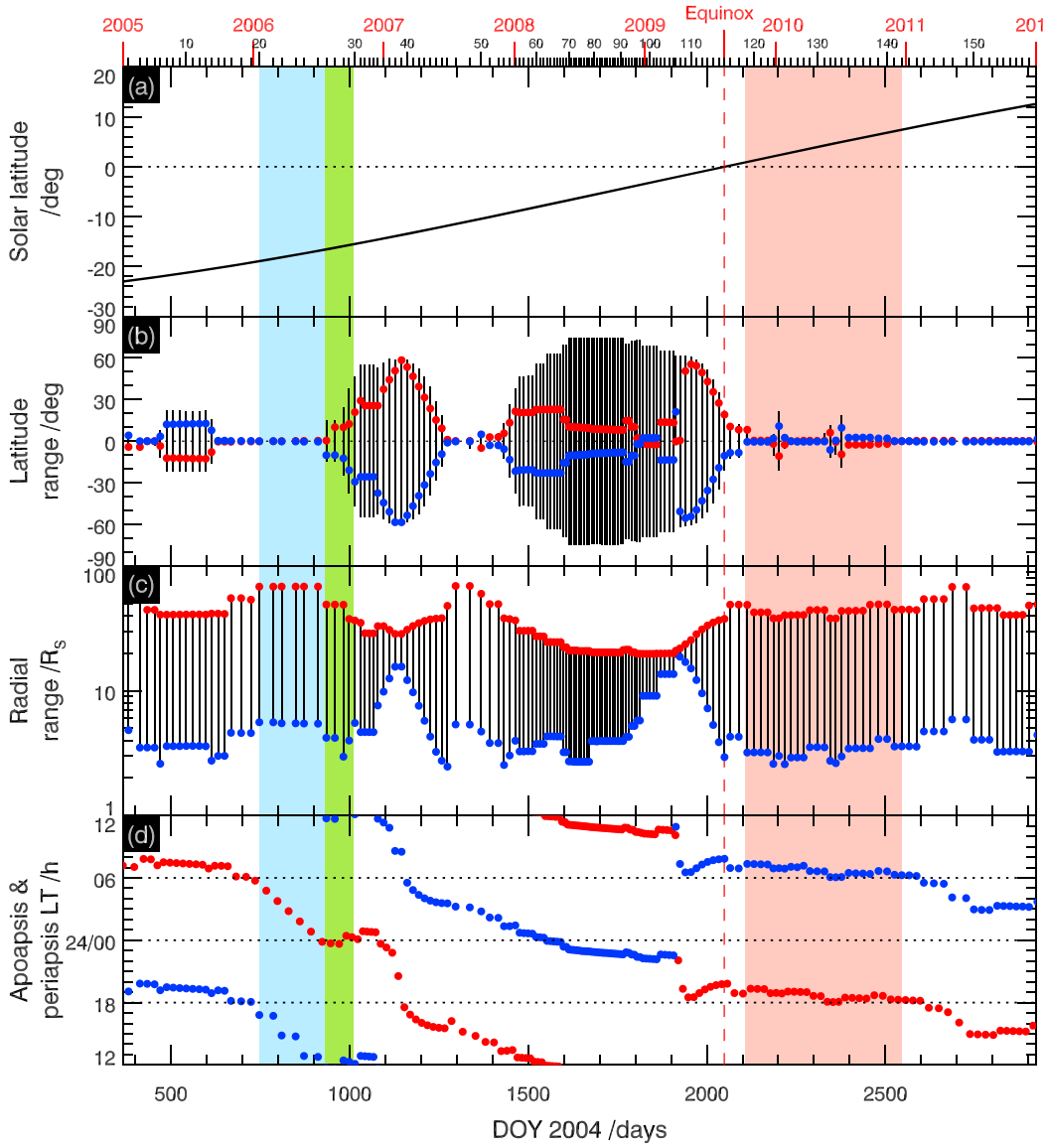

Figure 1. Details of Saturn's seasons and Cassini's orbits from the start of 2005 to the end of 2011, corresponding to $t = 366 - 2922$ days as marked at the bottom of the figure such that $t = 0$ days corresponds to 00 UT on 1 January 2004. The start of each year is marked in red at the top of the plot, while Cassini Rev numbers, defined from apoapsis to apoapsis, are marked in black at the time of periapsis. Figure 1a shows the solar latitude (deg) over the interval with a vertical dashed red line plotted at equinox. Figure 1b shows the latitude range (deg) of each Cassini Rev, plotted at the time of periapsis, with red and blue circles indicating the latitude at apoapsis and periapsis, respectively. Figure 1c shows the radial range of each Rev (R_S) on a log scale, also plotted at periapsis. Figure 1d shows the LTs (hr) of apoapsis (red circles) and periapsis (blue circles) for each Rev, plotted at the time of their occurrence.

2. Data Set and Physical Conditions

2.1. Data Intervals Employed

As indicated in section 1, the data analyzed in this paper are drawn from the catalogue of tailward propagating (plasmoid) and planetward propagating (dipolarization) reconnection-related events determined by Smith et al. (2016) from Cassini tail magnetic data obtained in 2006 and 2009/2010. Details of the spacecraft orbit, together with Saturn's prevailing season, which determine some basic properties of the event data, are shown in Figure 1. This figure spans the interval 2005 to 2011 inclusive as shown by the year boundaries at the top of the figure, corresponding to $t = 366$–$2{,}922$ days as shown at the bottom of the figure, where $t = 0$ day corresponds to 00 UT on 1 January 2004 (essentially the start of the Cassini

science mission). Cassini Revolution (Rev) numbers are also shown in black at the top of the figure, defined from apoapsis to apoapsis, plotted at the time of periapsis, and numbered every 10 Revs. The two intervals from which data have been employed are indicated by the colored vertical bars, the blue and green bars (covering different latitude regimes as discussed below) spanning the early and central interval of 2006 (t = 749–1,011 days corresponding to Revs 20–29), and the red bar the later post equinox interval of 2009 and the whole of 2010 (t = 2,107–2,544 days corresponding to Revs 118–141). Figure 1a shows the solar latitude at Saturn indicative of Saturn's seasons, which passes through zero from late southern summer to early northern spring at vernal equinox in August 2009, indicated by the vertical red dashed line. The solar latitude varied between −19° and −16° during the first (pre-equinox) interval corresponding to late southern summer, with the consequence that the tail plasma sheet was displaced significantly north of the planetary equatorial plane by the solar wind flow beyond a hinge point at ~29 R_S (e.g., Arridge et al., 2008). During the second (post equinox) interval the solar latitude varied between +1° and +7° corresponding to early northern spring, such that the tail plasma sheet was initially located close to the equatorial plane, becoming modestly displaced into the southern hemisphere later in the interval.

Figures 1b–1d show Cassini orbital parameters that determine and limit the nature of the event data. Specifically, Figure 1b shows the latitude range spanned on each Rev, plotted at periapsis, with red and blue circles showing the latitudes of apoapsis and periapsis, respectively. Figure 1c similarly shows the radial range on each Rev in Saturn radii (R_S, equal to 60,268 km) on a log scale, also plotted at periapsis, while the red and blue circles in Figure 1d show the LT of apoapsis and periapsis, respectively, plotted at the time of their occurrence. Figures 1b–1d show that during the 2006 interval the orbits were initially near equatorial with apoapsides in the range ~35–70 R_S, initially located in the dawn sector before moving towards midnight. Given the season shown in Figure 1a, this means that the nightside trajectory during this interval was typically located significantly south of the north displaced plasma sheet. After the periapsis of Rev 26, however, the orbit became modestly inclined with respect to the equatorial plane with apoapsis in the northern hemisphere, which brought the spacecraft into closer contact with the plasma sheet, as shown previously by Jackman et al. (2016). For this reason, as in Jackman et al. (2016) and Smith et al. (2016), the 2006 data have been divided into two intervals, corresponding to the earlier interval of near-equatorial orbits (t = 749 − 931 days corresponding to Revs 20–25), shown by the blue bar in Figure 1, and the later interval of inclined orbits (t = 931 − 1, 011 days corresponding to Revs 26–29), shown by the green bar in Figure 1. During this later interval apoapsis was located close to midnight, such that, overall, the 2006 data span from premidnight to predawn.

Figure 1b also shows that during the 2009/2010 interval the orbits were closely equatorial, with a few individual Revs making modest excursions out of the equatorial plane, such that given the near-equinoctial conditions prevailing, close contact was maintained with the plasma sheet throughout, as previously shown by Smith et al. (2016). These data are therefore considered as a whole, as indicated by the red bar in Figure 1. Figures 1c and 1d also show that apoapsis was consistently located in the range ~40–50 R_S in the dusk and postdusk sectors, such that most of the tail events were observed inbound from apoapsis in the dusk to premidnight region. Nightside observations were terminated at the end of 2010 as the LT of apoapsis rotated further into the predusk and dayside sector.

2.2. Event Examples and Locations

Examples of reconnection events in the Smith et al. (2016) catalogue examined here are shown in Figure 2. The radial B_r, colatitudinal B_θ, and azimuthal B_φ magnetic field components in spherical polar coordinates referenced to Saturn's northern spin/magnetic axis are plotted versus time over 1-hr intervals centered near the event onset time, for a dipolarization in Figures 2a–2c and for a plasmoid in Figures 2d–2f. Specifically, the dipolarization was observed on Rev 28 on 7 September 2006 (green interval in Figure 1), while the plasmoid was observed on Rev 121 on 18 November 2009 (red interval in Figure 1). Information on the spacecraft location, specifically the radial distance, LT, and latitude, is given at 10-min intervals beneath each panel. The start and end times of each event determined by Smith et al. (2016) from variations in the colatitudinal field component are marked by the pairs of red vertical dashed lines in each panel. The dipolarization is marked by a small negative (northward) perturbation followed by a large positive (southward) deflection (Figure 2b), while the plasmoid is marked by a small positive perturbation followed by a large negative deflection (Figure 2e). Large concurrent variations also occur in the radial component in both cases

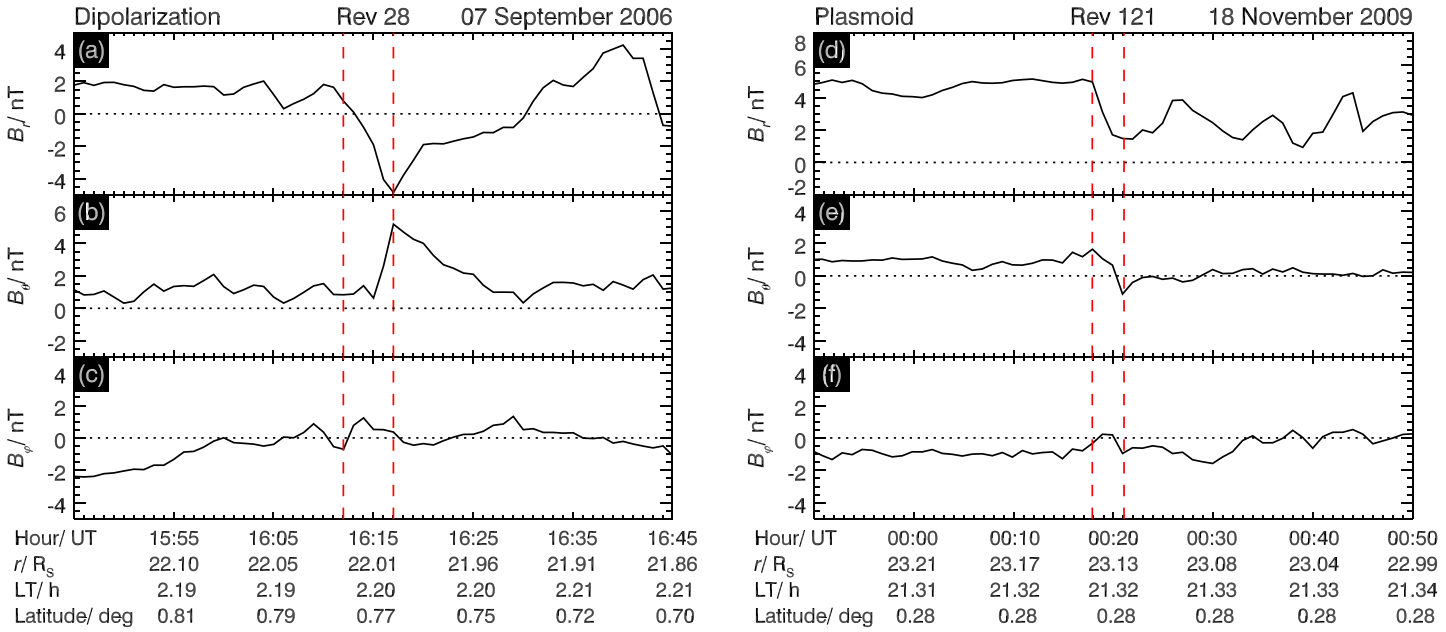

Figure 2. Examples of a dipolarization and a plasmoid event determined by Smith et al. (2016) from variations in the colatitudinal magnetic field component. In each case we show the three field components in spherical polar coordinates referenced to the northern planetary spin/magnetic axis, radial B_r, colatitudinal B_θ, and azimuthal B_φ, plotted over a 1-hr interval centered near the event onset time. The dipolarization in Figures 3a–3c was observed on Rev 28 on 7 September 2006, while the plasmoid in Figures 3d–3f was observed on Rev 121 on 18 November 2009, with start and end times indicated by the red vertical dashed lines in each panel. Data beneath each panel show the UT time (hr:min) at 10-min intervals, together with the corresponding radial distance (R_S), LT (decimal hour), and latitude (deg).

(Figures 2a and 2d), with smaller perturbations in the azimuthal component (Figures 2c and 2f). The durations of the events are ~5 min for the dipolarization and ~3 min for the plasmoid.

The locations of the events identified by Smith et al. (2016) are shown in Figure 3, specifically at the event start times (typical durations ~5–10 min), where we show all of the events irrespective of whether tailward or planetward propagating, that is, plasmoids or dipolarizations. As we demonstrate below, the spatial distributions of both types of event, determined principally by the orbit characteristics (Figure 1), are very similar to each other. The locations are shown in kronographic stationary (KGS) coordinates, where the *Z* axis is aligned with the planet's northern spin/magnetic axis, the *X*-*Z* plane contains the Sun (positive *X*), and *Y* completes the right-handed set pointing from dawn to dusk. Figure 3a shows the locations projected onto the planetary equatorial *X*-*Y* plane, while Figure 3b similarly shows them projected onto the noon-midnight *X*-*Z* plane, where blue, green, and red points correspond to the three temporal intervals shown by the similarly colored bars in Figure 1. We note that the search for events was confined to the nightside hours at radial distances beyond 15 R_S but was not otherwise restricted, other than to exclude data obtained close to magnetopause encounters and to special spacecraft maneuvers. Dashed lines show the magnetopause intersections with the corresponding planes from the model of Pilkington et al. (2015), specifically for solar wind dynamic pressures of 0.01 and 0.1 nPa, spanning the usual range.

Figure 3 shows that the events span the range of nightside LTs from dusk to predawn, though with greatest numbers in the postdusk and midnight sectors, due principally to the orbital coverage of the spacecraft. Colored shaded regions bounded by dotted lines in Figure 3b also show the range of locations of the center of the plasma/current sheet in the noon-midnight meridian during the intervals corresponding to the similarly colored data points and to the bars in Figure 1. These were computed from the Arridge et al. (2008) model, using a current sheet hinging distance of 29 R_S. As indicated in section 2.1, this shows that the equatorial orbits in the initial interval of 2006 (blue) were generally located far south of the current sheet center, except at small radial distances. The later tilting of the orbit apoapsis into the northern hemisphere in 2006 (green) brought the spacecraft into closer contact with the similarly tilted current sheet and with the region north of the current sheet. The near-equatorial orbits in 2009/2010 were also located close to the post equinox near-equatorial plasma sheet, with a few excursions both north and south.

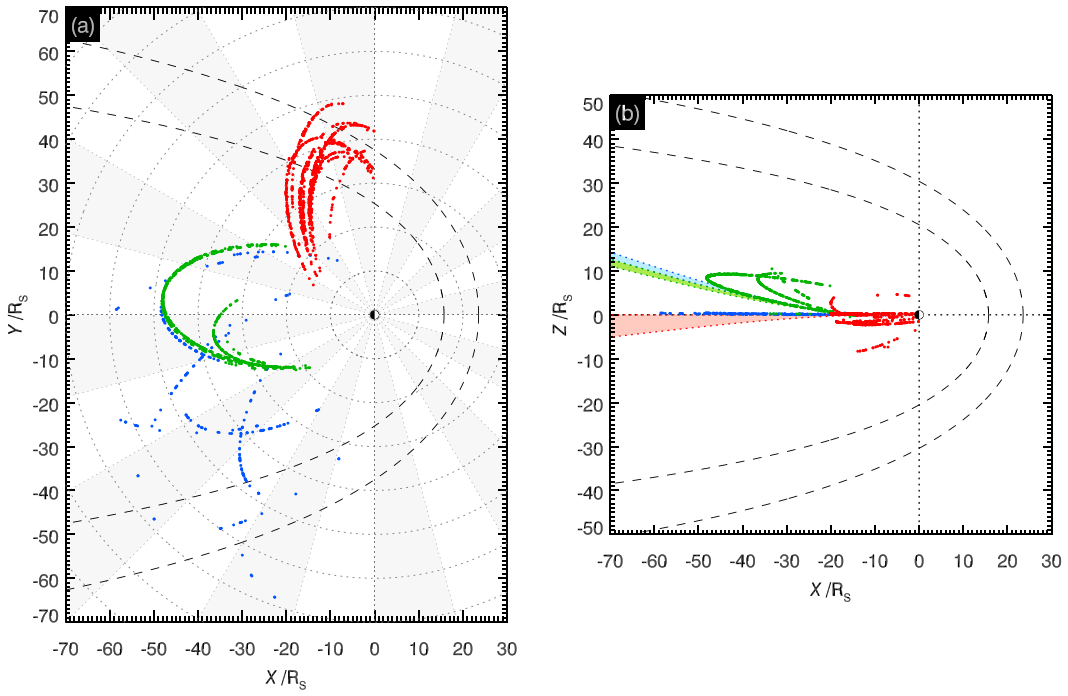

Figure 3. Locations of Smith et al. (2016) reconnection events in KGS coordinates (R_S), projected onto the *X-Y* plane in Figure 3a and onto the *X-Z* plane in Figure 3b. Events from the 2006 equatorial Revs are shown in blue, from the 2006 inclined events in green, and from the 2009/2010 Revs in red, matching the colored bars in Figure 1. Black dashed lines in each panel show the Pilkington et al. (2015) model magnetopause for solar wind dynamic pressures of 0.01 and 0.1 nPa (outer and inner lines, respectively). Dotted circles in Figure 3a indicate radial intervals of 10 Rs, while dotted lines indicate 1-hr LT intervals, with every other hour shaded light gray. In Figure 3b the range of locations of the tail current sheet center in the noon-midnight meridian is also indicated for each interval by the correspondingly colored areas bounded by dotted lines, calculated using the Arridge et al. (2008) model with a 29 R_S hinging distance.

Further information on the spatial distribution of the events is shown in histogram format in Figure 4, where data for the tailward and planetward events are shown separately in Figures 4a–4c and 4d–4f, respectively. Specifically, we show histograms of radial distance (Figures 4a and 4d), LT (Figures 4b and 4e), and north-south displacement from the center of the current sheet (Figures 4c and 4f), each shown as a percentage of the total number of tailward or planetward events (given above each row of figure panels) for each nonoverlapping histogram bin. Note the different percentage scales employed in the radial, LT, and north-south displacement histograms. We again focus on event start times, and the position of the current sheet center has been estimated from the Arridge et al. (2008) model. The color-coded numbers given in the upper right corners of each panel indicate the median values of the similarly colored histogram data denoting event types, as will now be outlined.

As indicated in section 1, following Smith et al. (2016), events are categorized according to whether they are isolated, that is, separated from others by at least 3 hr, or occur in a cluster with individual events (either tailward or planetward) separated by less than 3 hr. The choice of 3 hr was made on the basis of scaling the 30 min used in related terrestrial studies by Slavin et al. (1993). Clusters are taken to represent a single episode of ongoing reconnection with a start time given by the start of the initial event in the cluster. The mean total number of events in a cluster is ~5, with a mean time between events of a little less than ~1 hr, and a mean duration of ~3 hr, which we note is a modest fraction of an ~10.7-hr PPO period. The number of individual reconnection episodes in the data set is thus taken to be given by the sum of the number of isolated events plus the number of clusters. Events in the data set are correspondingly separated into three types, isolated events, primary cluster events being the first event in a cluster, and subsequent secondary cluster events, each of which types may be either tailward or planetward in nature. In Figure 4 the dark blue areas correspond to the occurrence histograms of isolated events. The medium blue areas plotted above these correspond to the primary cluster events, so that the overall histograms formed by the dark and

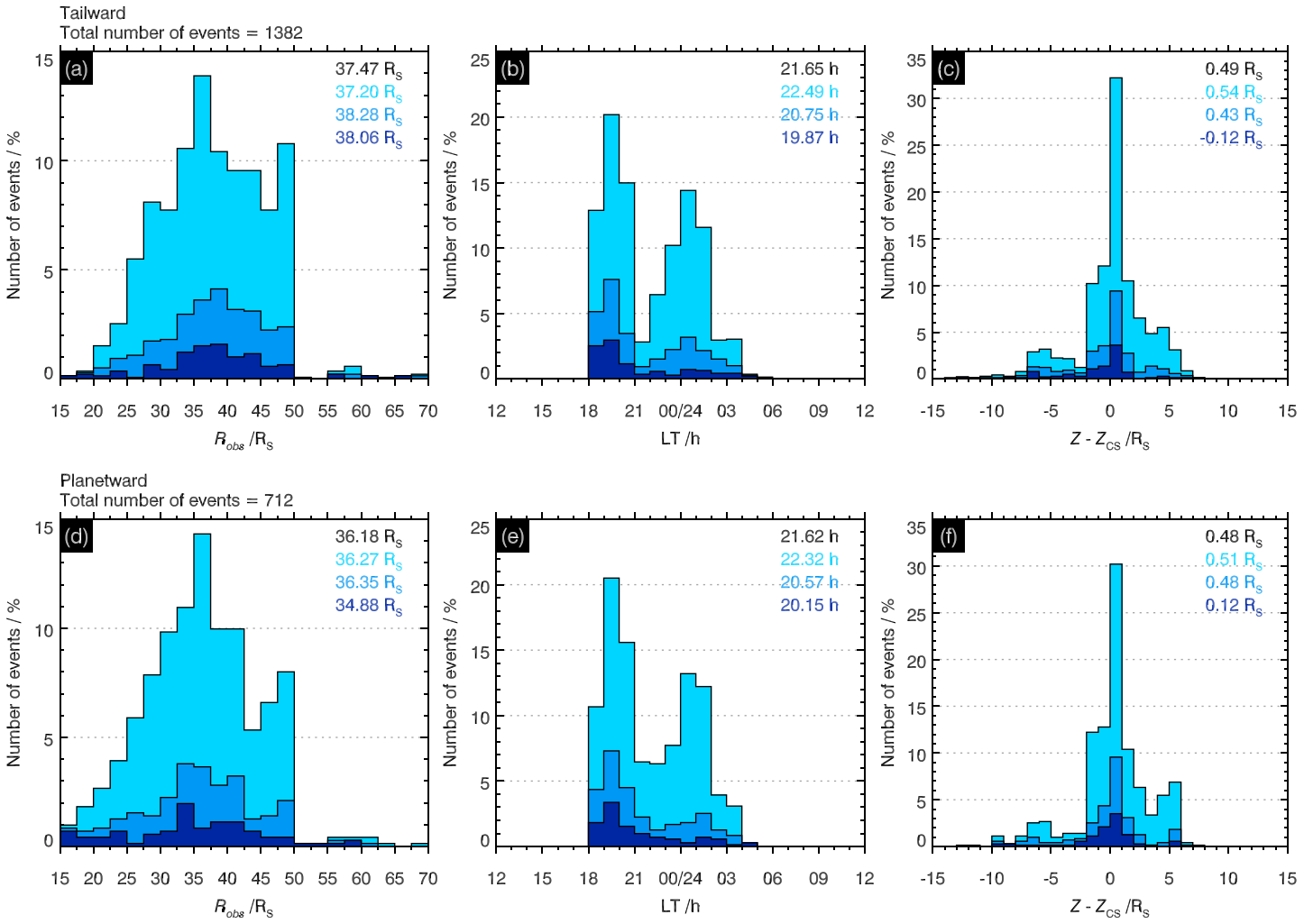

Figure 4. Occurrence frequency histograms showing spatial information for tailward events (Figures 4a–4c) and planetward events (Figures 4d–4f). Figures 4a and 4d show histograms of the radial distance (R_S), Figures 4b and 4e the LT (hr), and Figures 4c and 4f the north-south displacement of the spacecraft located at Z from the center of the Arridge et al. (2008) current sheet located at Z_{CS} (R_S). The frequency for each nonoverlapping bin is given as a percentage of the total number of events indicated above each row of panels (see also Table 1), with differing percentage scales being employed for the radial, LT, and north-south displacement plots. Histograms for the isolated events are shown by the dark blue area, for primary cluster events by the medium blue area, and for secondary cluster events by the light blue area. The medium and dark blue areas combined thus show the occurrence histograms for the independent reconnection episodes, while the overall histograms correspond to the totality of the events. The median values for each type of event are shown with the same color scheme in the top right of each panel, with the median for all types of event in black.

medium blue areas combined correspond to the sum of the isolated and primary cluster events, representing the distribution of individual reconnection episodes. The light blue areas plotted above the medium blue areas then correspond to the secondary cluster events, so that the overall histograms correspond to the totality of the events, either tailward or planetward.

Overall, these histograms show that the events were principally observed at radial ranges between ~25 and ~50 R_S, span LTs between dusk and predawn (to ~4-hr LT, apart from a few events lying closer to dawn) with a relative minimum premidnight, and at north-south distances up to ±7 R_S either side of the current sheet center, all mainly determined by the nature of the spacecraft orbit. In particular, the events at larger negative Z-Z_{CS} values were observed principally during the initial equatorial orbit interval in 2006, those at larger positive Z-Z_{CS} values during the following inclined orbit interval in 2006, while those within ±2 R_S of the current sheet center correspond principally to a combination of events observed during the later interval in 2006 and those in 2009/2010. It can be seen that the events in all categories, isolated, primary cluster, and secondary cluster, follow the same basic trends, though with an apparent preference for isolated events to

Table 1
Breakdown of Event Numbers in the Smith et al. (2016) Catalogue by Type and Observation Interval

Interval	2006 equatorial orbits[a]		2006 inclined orbits[b]		2009/2010 near equatorial[c]		All intervals	
Event type	Tailward	Planetward	Tailward	Planetward	Tailward	Planetward	Tailward	Planetward
Isolated events[d]	34	17	13	10	96	51	143	78
Primary cluster events[e]	49	19	73	31	138	72	260	122
Secondary cluster events[f]	108	54	416	223	455	235	979	512
All events	191	90	502	264	689	358	1382	712
Independent reconnection episodes[g]	119		127		357		603	
Time in viewing region (days)[h]	131		76		207		415	
Independent episodes per 10.7 hr[i]	0.40		0.75		0.77		0.65	
Mean events per cluster[j]	3.4		7.1		4.3		4.9	

[a]Revs 20–25. [b]Revs 26–29. [c]Revs 118–141. [d]Events separated from others by more than 3 hr. [e]First of a cluster of events separated from each other by 3 hr or less. [f]Subsequent events in a cluster, after the first. [g]Sum of isolated plus primary cluster events for tailward and planetward events combined. [h]From Table 1 of Smith et al. (2016). [i]Mean number of independent reconnection episodes per nominal 10.7-hr PPO period. [j]Total number of primary plus secondary cluster events divided by the total number of primary cluster events (tailward and planetward combined).

occur at earlier LTs for both tailward and planetward events. It can also be seen that the tailward and planetward events follow similar spatial distributions, though with a modest tendency for planetward events to be relatively more numerous (in percentage terms) in the inner part of the tail (within ~25 R_S), and tailward events in the outer part (outside ~40 R_S), as might be expected. Overall, however, both tailward and planetward events are observed with comparable percentages over the whole range of observations. However, we note that the absolute number of planetward events is significantly smaller than the number of tailward events by a factor of ~2 in all categories, with an overall tailward/planetward ratio of ~1.9.

In Table 1 we provide a breakdown of total event numbers by event type and by data interval. Toward the bottom of the table we also give the numbers of individual reconnection episodes in each interval, consisting of the sum of the isolated and primary cluster events for both tailward and planetward categories. We also give the number of days spent by the spacecraft within the *viewing region* for each interval as quoted in Table 1 of Smith et al. (2016), this simply being taken to be the time spent beyond 15 R_S radial distance at nightside LTs between dusk and dawn. Dividing the two yields the number of episodes per PPO period, taken for simplicity to be 10.7 hr, shown near the bottom of Table 1. The number varies between ~0.4 for the initial interval in 2006 with observations generally at large displacements south of the current sheet center and ~0.8 for the 2009/2010 data obtained closer to the center. The overall number is ~0.65. As indicated in section 1, if these events are associated with large-scale magnetospheric dynamic activity, such values suggest a principal (but not necessarily exclusive) connection with the PPO-related events discussed, thus motivating investigation of related PPO event modulation. At the bottom of Table 1 we also give the mean number of events in the clusters in each interval, combining together both tailward and planetward events. As indicated in outline above, the mean number overall is 4.9 events per cluster (primary plus secondary), similar to the 4.3 events for the 2009/2010 data comprising half the event sample.

2.3. PPO Effects on the Tail Current Sheet

Properties of the PPO systems relevant to issues of plasma sheet stability are illustrated in Figure 5, where Figures 5a–5c refer to the northern PPO system and Figures 5d–5f to the southern PPO system, following the previous discussions by Provan et al. (2012), Hunt et al. (2014), Jackman et al. (2016), and Cowley et al. (2017). Figures 5a and 5d show the PPO-related driving thermospheric-ionospheric flows (arrowed red lines) and associated perturbation magnetic fields (arrowed blue lines) in the northern and southern polar hemispheres, respectively, in views looking down from the north (through the planet in the case of the southern hemisphere). These figures also show the northern (N) and southern (S) azimuthal phase angles $\Psi_{N,S}$ used to define azimuthal position with respect to these systems. At lower latitudes the perturbation fields are directed from $\Psi_{N,S} = 180°$ toward $\Psi_{N,S} = 0°$ in both systems and close in the opposite direction over the corresponding poles. Representations of the extended magnetospheric perturbation fields in the $\Psi_{N,S} = 0° - 180°$ meridian plane (arrowed blue lines) are shown for the two systems in Figures 5b

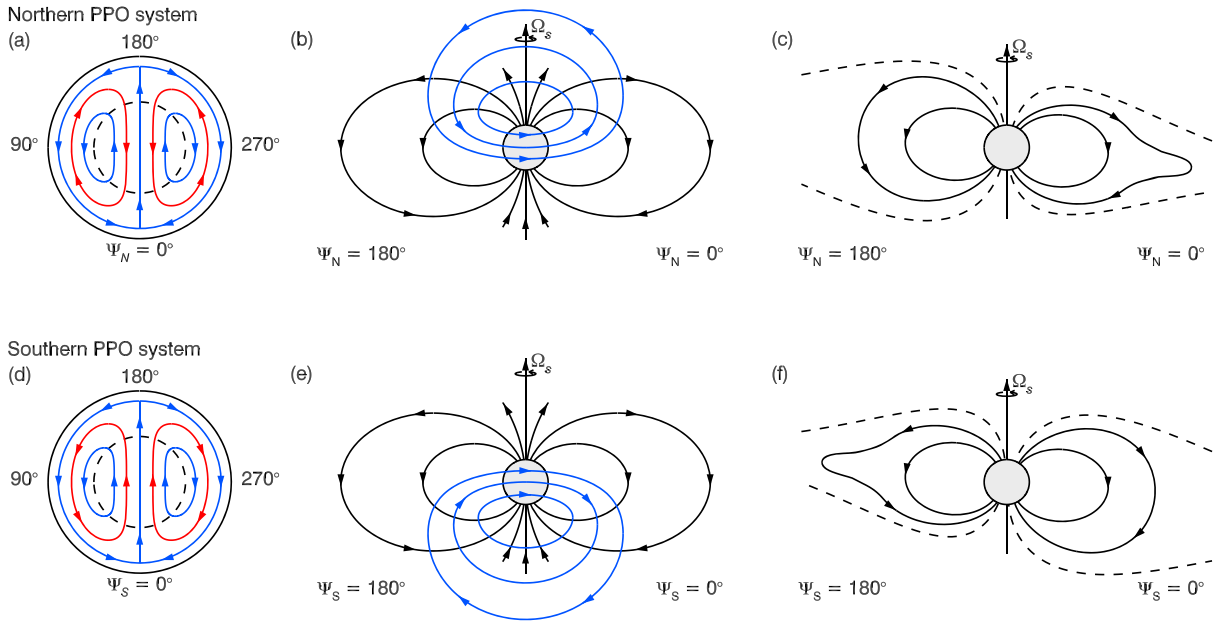

Figure 5. Sketches of Saturn's northern (Figures 5a–5c) and southern (Figures 5d–5f) PPO magnetic perturbations with the blue arrowed lines showing the perturbation field and the red arrowed lines showing the associated atmospheric/ionospheric flow. Figures 5a and 5d look from the north down onto Saturn's ionosphere along the spin/dipole axis (through the planet in the case of Figure 5d), with the azimuthal PPO phase systems shown such that $\Psi_{N,S} = 0°$ is at the bottom in each. Figures 5b and 5e show the magnetic perturbations in a meridional view such that $\Psi_{N,S} = 0°$ toward the right and $\Psi_{N,S} = 180°$ toward the left for each panel, with the background dipole field now shown via black arrowed lines. Figures 5c and 5f show the thickening/thinning and north/south displacements of the current sheet field lines caused by the PPOs (based on Andrews et al., 2010, Provan et al., 2012, and Cowley et al., 2017).

and 5e, where the arrowed black lines indicate the background magnetic field, approximately axisymmetric about the vertical planetary spin/magnetic axis. The perturbations away from this meridian are to a first approximation given simply by displacing the blue field loops directly into or out of the plane of the diagram. With increasing time these systems rotate about the axis with close but generally distinct periods typically within ~1% of 10.7 hr. The effects of these fields on the plasma/current sheet are illustrated in Figures 5c and 5f, shown for $\Psi_{N,S} = 0°$ and $\Psi_{N,S} = 180°$ for convenience of drawing on either side of the planet, though referring here principally to nightside LTs. The arrowed black lines show perturbed current sheet field lines, bounded by the black dashed line. Two principal effects are shown. The first is associated with the radial component of the perturbation field, which causes the current sheet to displace to the south at $\Psi_{N,S} = 0°$ where the perturbation field points radially outward in the same sense as the northern lobe field and to displace to the north at $\Psi_{N,S} = 180°$ where the perturbation field points radially inward in the same sense as the southern lobe field. The second is associated with the colatitudinal component of the perturbation field, which augments the southward planetary field in the current sheet at $\Psi_N = 180°$ and $\Psi_S = 0°$ where the perturbation field is positive, causing the plasma/current sheet to thicken, but diminishes the planetary field at $\Psi_N = 0°$ and $\Psi_S = 180°$ where it is negative, causing it to thin. For the north-south displacements the effect of the two systems are in the same sense and will add when they are in phase but are in opposite senses and will part cancel when they are in antiphase, while for thickening and thinning the effect of the two systems is in the same sense and will add when they are in antiphase but are opposite and will part cancel when they are in phase. These effects have been well demonstrated in studies of nightside current sheet data (Cowley et al., 2017; Cowley & Provan, 2017; Provan et al., 2012; Thomsen et al., 2017). We note that it is principally the effects associated with the colatitudinal perturbation field that are likely to be germane to the issue of current sheet stability, with the sheet being less stable to reconnection for $\Psi_N = 0°$ and/or $\Psi_S = 180°$ when it is thin and threaded by a weaker north-south field, than for the antiphase conditions when the sheet is thick and threaded by a stronger north-south field. A related idea was previously proposed by Milan et al. (2009) to explain the enhanced stability of the Earth's nightside current sheet during intervals of enhanced ring current, due to the effect of the north-south fringing field of the latter current system.

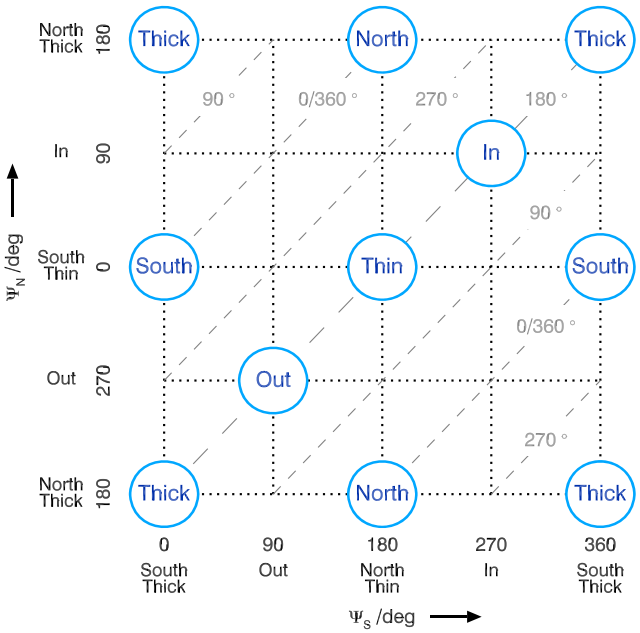

Figure 6. Diagram showing the expected perturbations of the tail plasma/current sheet associated with the northern and southern PPO phases. The vertical axis shows the northern phase Ψ_N plotted between −180° and 180° together with expected northern system effects, north-south displacements, thickening or thinning, and inward or outward radial displacements, while the horizontal axis similarly shows the southern phase Ψ_S plotted between 0° and 360° and the related expected southern system effects. Dual phases where both systems act in concert to produce a given effect are indicated in circles on the phase grid. Labeled gray dashed lines indicate lines of constant beat phase, defined as the northern phase minus the southern phase, along which the two phases approximately travel with time during a rotation (given near-equal periods).

A second potentially relevant factor concerns associated radial displacements of the plasma sheet field lines during the PPO cycle. As shown by the arrowed red lines in Figures 5a and 5d, the PPO systems are driven by rotating twin vortices in the two polar thermospheres-ionospheres, whose flows are transmitted along the planetary field lines into the magnetosphere (Jia et al., 2012). For the northern system in Figure 5a the flows are directed equatorward, corresponding to radially inward in the magnetosphere, during the half-cycle centered on Ψ_N = 0°, but are directed poleward, corresponding to radially outward in the magnetosphere, during the half-cycle centered on Ψ_N = 180°. As the subcorotating magnetospheric plasma then rotates clockwise relative to the PPO system, flux tubes will be displaced radially inward during the first interval, reaching maximum equatorward displacement at Ψ_N = 90°, and will be displaced outward during the second, reaching maximum poleward displacement at Ψ_N = 270°. Similarly for the southern system in Figure 5d, the flows are directed poleward, corresponding to radially outward in the magnetosphere, during the half-cycle centered on Ψ_S = 0°, but are directed equatorward, corresponding to radially inward in the magnetosphere, during the half-cycle centered on Ψ_S = 180°. As the subcorotating magnetospheric plasma then rotates clockwise relative to this PPO system, flux tubes will be displaced radially outward during the first interval, reaching maximum poleward displacement at Ψ_S = 90°, and will be displaced radially inward during the second, reaching maximum equatorward displacement at Ψ_S = 270°. Such PPO-related modulation in latitude of the southern auroral current systems has been demonstrated directly by Hunt et al. (2014) in the case of the southern PPO system. Again, we may expect reconnection with pinch-off of plasmoids to be favored when the plasma and flux tubes are displaced radially outward at Ψ_N = 270° and/or Ψ_S = 90°, thus again favoring antiphase conditions, rather than when the plasma and flux tubes are displaced radially inward at Ψ_N = 90° and/or Ψ_S = 270°.

Following Jackman et al. (2016), these discussions are summarized by the diagram in Figure 6, where the effect of each system on the plasma/current sheet, north or south displacements, thickening or thinning, and inward or outward radial field line displacements are indicated in the Ψ_N − Ψ_S phase plane. Specifically, the northern phase Ψ_N (plotted for convenience between −180° and 180°) is shown on the vertical axis, and the southern phase Ψ_S (plotted between 0° and 360°) is shown on the horizontal axis, with the associated effects on the current sheet being indicated on each axis at the appropriate phases. Within the grid we then indicate in circles the dual phases for which both systems act to reinforce a particular modulation, with north-south cyclic modulations being dominant when the systems are in phase (moving with time approximately along 45° lines in the phase plane connecting *South* and *North*, shown by the gray dashed lines marked with beat phase 0°/360°), and thickening-thinning and inward-outward cyclic modulations being dominant when the systems are in antiphase (moving with time approximately along 45° lines connecting *Thick*, *Out*, *Thin*, and *In*, shown by the gray dashed lines marked with beat phase 180°). Reconnection events are expected to be favored under Out and Thin conditions in the lower center-left region of the plot. This expectation is examined in section 3 using the events in the Smith et al. (2016) catalogue.

2.4. PPO Properties During the Event Intervals

Properties of the PPOs during the event intervals are shown in Figure 7 in a similar format and over the same interval as in Figure 1, based on the results of Andrews et al. (2012) and Provan et al. (2013). Figure 7a shows the periods of the northern (blue) and southern (red) PPO systems, while Figure 7b shows their beat period τ_B, given by $\tau_B^{-1} = \left|\tau_N^{-1} - \tau_S^{-1}\right|$, on a log scale. Figure 7c shows the amplitudes of the northern (blue) and southern (red) PPO perturbation fields, specifically of the near-equatorial quasi-uniform field within the

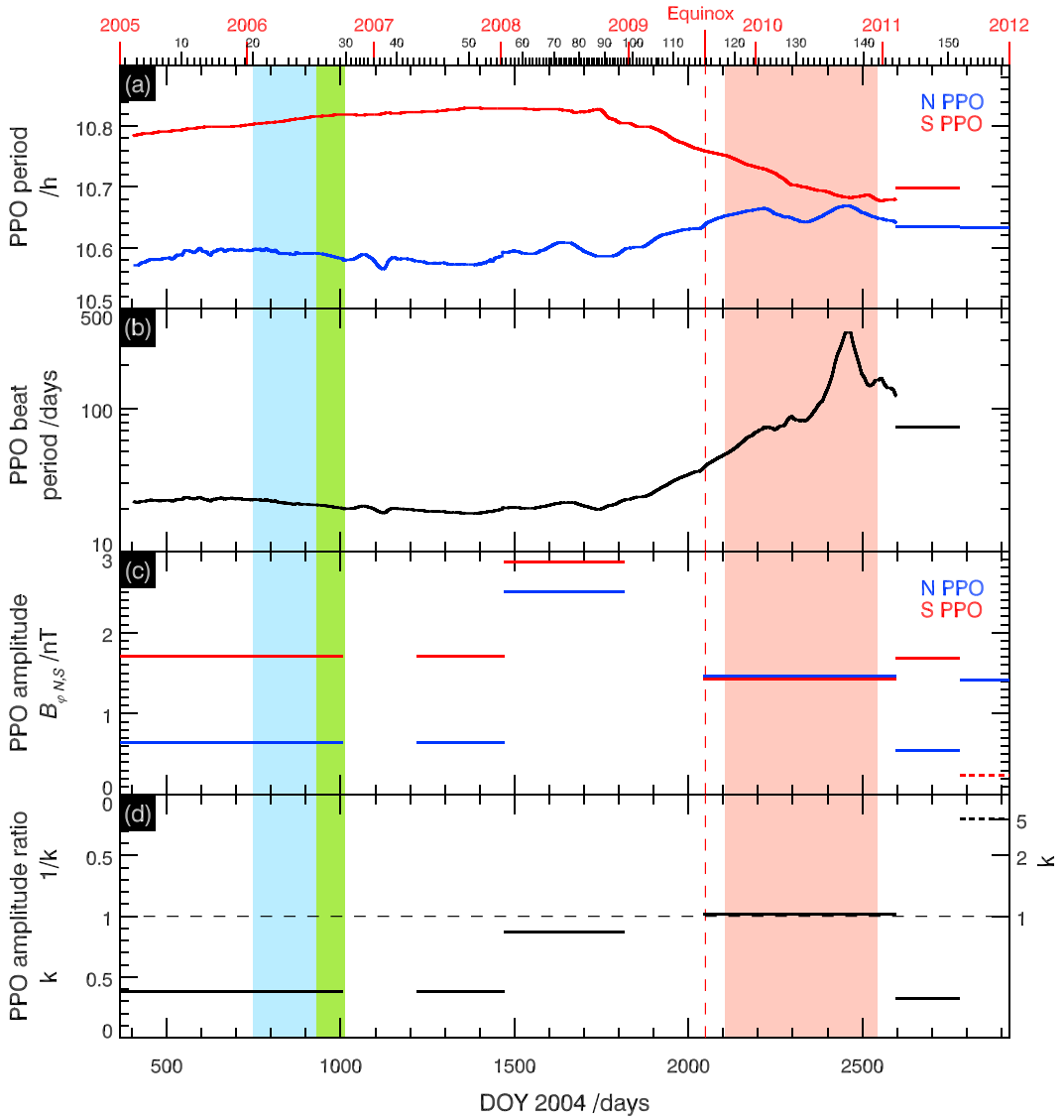

Figure 7. PPO conditions spanning the same interval as Figure 1, with the same Rev and year boundary markers detailed at the top of the plot. Figure 7a shows the periods (hr) of the north (blue) and south (red) PPO systems, while Figure 7b shows their beat period (days) on a log scale. Figure 7c shows the amplitudes (nT) of the azimuthal components of the PPOs within the equatorial region, where a dashed line upper limit for the southern amplitude has been used during an interval in late 2011 when the southern PPO was not discernable relative to the northern (maximum amplitude of one fifth the northern amplitude). Figure 7d shows the north/south amplitude ratio *k*, shown directly in the lower half of the panel, and as 1/*k* in the upper half panel, with a nonlinear *k* scale being shown on the right hand axis.

quasi-dipolar region (dipole $L < \sim 15$) of the magnetosphere (see Figures 5b and 5e), and Figure 7d shows their ratio k (north amplitude divided by south amplitude), where k is shown directly in the lower half panel and $1/k$ in the upper half (with additional nonlinear k scale on the right hand axis), thus appropriately covering the whole range $0 \leq k \leq \infty$.

It can be seen that the two periods were well separated during the 2006 study interval, ~10.6 hr for the northern system and ~10.8 hr for the southern, with a beat period of ~20 days. With orbital periods of ~20–30 days during this interval, significant variations of relative PPO (beat) phase occurred on each Rev, and from Rev to Rev. We also note that the southern system was dominant during this late southern summer interval, with a north/south ratio k of ~0.38, such that the tail current sheet may be expected to respond more to the phase of the southern system than the northern. Nevertheless, modulation by the northern system may still produce significant effects, with a sum/difference (in phase/antiphase) amplitude ratio $(1 + k/1 - k)$ of ~2.2.

During the post equinox 2009/2010 study interval, however, the two periods moved slowly toward a near-common period of ~10.7 hr near the end of 2010, such that the beat period increased from ~50 to over ~100 days. With orbital periods remaining close to ~20 days during the interval, this implies that the beat phase varied only slowly within a restricted range during each Rev, though with full coverage of relative system phases over the ~437-day 2009/2010 data set as a whole. We also see that the amplitudes of the two systems were very close to each other during this interval with north/south ratio $k \sim 1.02$, due to a small fall in the amplitude of the southern system compared with 2006, but a proportionately larger increase in the amplitude of the northern system. This implies that the amplitudes of the field perturbations were essentially doubled when the effects were in the same sense as each other and canceled to near zero when they were opposite.

2.5. PPO Phases of Nightside Reconnection Event Onsets

The Smith et al. (2016) catalogue provides the time and position of the start and end of both tailward and planetward propagating reconnection signatures based on the perturbations observed in the colatitudinal field component, of which we focus here on the start parameters, specifically the observed start time T_{obs}, spacecraft radial distance R_{obs}, and azimuth with respect to noon φ_{obs}. However, as pointed out by Jackman et al. (2016), these do not necessarily correspond precisely to the reconnection event onset itself, which, in general, will have begun at some earlier time T_{rec}, and at a radial distance R_{rec}, which is smaller than R_{obs} for tailward propagating events and larger than R_{obs} for planetward propagating events. In the absence of detailed information we assume near-radial propagation throughout, so that φ_{rec} is taken to be equal to φ_{obs}. In section 2.6 below we will outline simple algorithms from which we estimate the reconnection times and radial distances, and their uncertainties, from the observed values for both types of event, and will show that the differences are not generally of major significance.

Given the reconnection time T_{rec}, we then, in general, know the orientation of the two PPO systems at that time from the analysis provided by Andrews et al. (2012), which spans both study intervals, in 2006 and 2009/2010. These are given by the phase angles $\Phi_{N,S}$ (T_{rec}), the azimuths with respect to noon of the $\Psi_{N,S} = 0°$ meridians, taken positive in the sense of planetary rotation. The only exception to this statement arises for the northern PPO phase during the 2006 interval, which was not well determined due to its low amplitude relative to the southern PPO modulations (Figure 4c), for which we instead use the northern SKR phase determined by Lamy et al. (2011) on the basis that we expect $\Phi_N \approx \Phi_{N\ SKR}$ during this interval (see discussion in section 2.1 of Jackman et al. (2016)). While the phases $\Phi_{N,S}$ (t) give the orientation of the PPO systems relative to noon in the inner quasi-dipolar part of the magnetosphere, the reconnection events we study here are all located in the tail beyond this region, for which we must apply a phase correction due to the finite speed of radial propagation of the PPO modulation downtail at typically ~200 km/s (Arridge et al., 2011; Provan et al., 2012). Beyond a radial distance of 12 R_S, therefore, corresponding approximately to the outer limit of the quasi-dipolar region, the radially retarded phase of the reconnection events is taken to be given by

$$\Phi^*_{N,S}(T_{rec}, R_{rec}) = \Phi_{N,S}(T_{rec}) - G(R_{rec} - 12), \tag{1}$$

where R_{rec} is in R_S and radial phase gradient $G = 3$ deg R_S^{-1} corresponding approximately to the above downtail speed. Given the observed reconnection events that occur typically ~20 R_S beyond the quasi-dipolar region (Figure 4), the ~60° phase retardations involved can be a reasonably significant fraction of a PPO cycle. If the observed events are large scale in nature, involving a significant fraction of the whole tail width, we might expect them to be best organized by the global orientation of the two PPO systems relative to the tail and hence by the retarded phase given by equation (1). On the other hand, if they are more local in nature, involving only some restricted sector of the tail in which they are observed, then we might expect them to be best organized by the local retarded PPO phases, which take account of the azimuth (LT) of the events, given by

$$\Psi^*_{N,S}(T_{rec}, R_{rec}, \varphi_{rec}) = \Phi^*_{N,S}(T_{rec}, R_{rec}) - \varphi_{rec}, \tag{2}$$

where as above we take $\varphi_{rec} = \varphi_{obs}$, defining the (retarded) azimuthal location of the event with respect to the two PPO systems as defined in Figure 5.

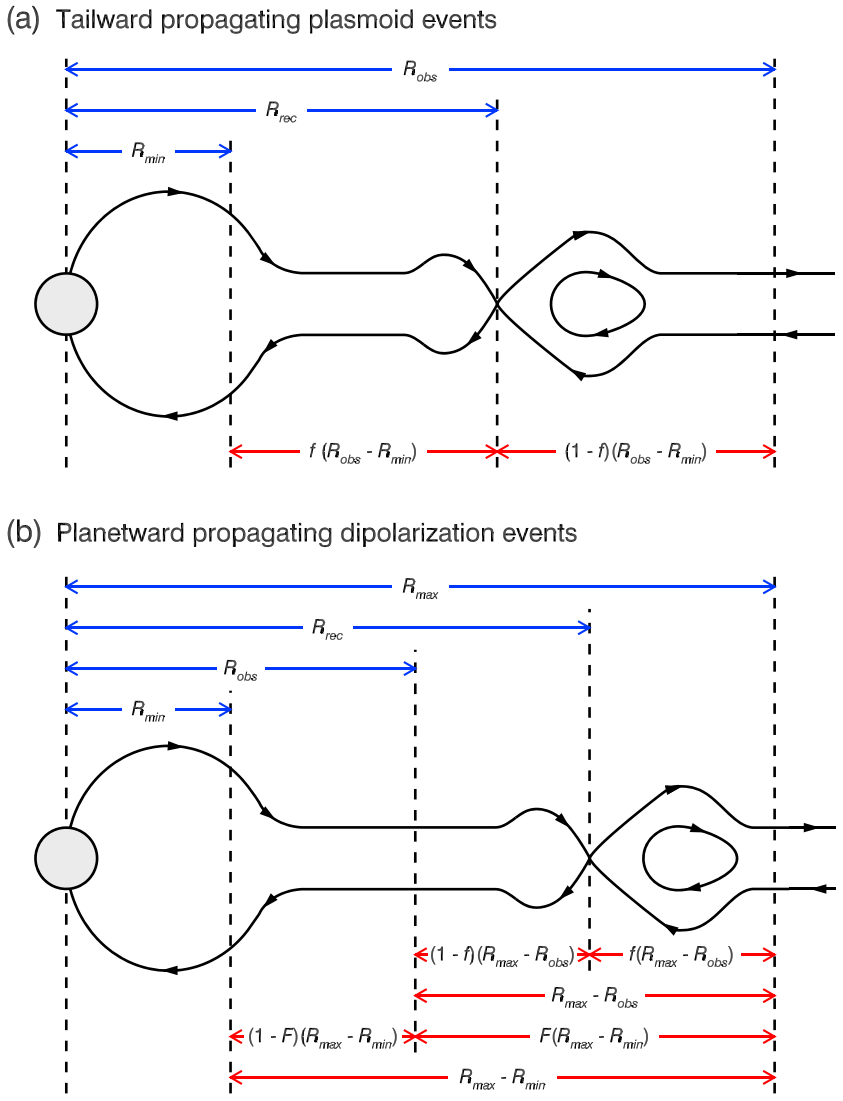

Figure 8. Schematics of the algorithms used to estimate the radial distance of reconnection onset, R_{rec}, from the radial distance of the observation, R_{obs}, for tailward directed plasmoid events (Figure 8a) and planetward directed dipolarization events (Figure 8b). Black arrowed lines show field lines on the nightside of Saturn, with vertical dashed lines indicating radial distances used in the algorithms discussed in section 2.6. Radial distances from the planet of relevant features are shown by blue arrowed lines above each diagram, while radial distances between these points are shown by red arrowed lines beneath.

2.6. Reconnection Onset Times and Distances

We now briefly consider the issue outlined above of determining the likely onset time and radial distance of a reconnection event, T_{rec} and R_{rec}, from the observed start times and positions, T_{obs} and R_{obs}. Diagrams are provided in Figure 8 illustrating the assumptions in the following algorithms. We begin with the more straightforward case of tailward propagating events (Figure 8a), which perforce must have originated at a smaller downtail radial distance than the observation point. Following Jackman et al. (2016), we note from Figure 4a that the vast majority of tailward events, more than ~95%, are observed at radial distances beyond ~25 R_S, so it is reasonable to suppose that an individual event observed beyond this distance was formed at a radial distance between the observation point and 25 R_S. That is, we can write

$$R_{rec} = R_{min} + f(R_{obs} - R_{min}) = R_{obs} - (1 - f)(R_{obs} - R_{min}), \quad (3)$$

for some fraction $0 \le f \le 1$, where R_{min} = 25 R_S (see Figure 8a). The onset time of the event is then given by

$$T_{rec} = T_{obs} - \left((1-f)(R_{obs} - R_{min})/V_{plas}\right), \tag{4}$$

where V_{plas} is the downtail speed of the plasmoid disturbance, taken to be 300 km/s based on the results of Jackman et al. (2014). Of course, for any individual event we have no way of knowing what the appropriate value of f may be. In the analysis given below we thus simply employ $f = 0.5$ as a fixed central value, in order to make some overall allowance for the radial displacement of the reconnection site away from the observation point. In section 3.2 we also examine f = 0.25 and 0.75, with results showing little sensitivity to the choice. Given median values $R_{obs} \approx 37$ R_S (Figure 4a), the estimated radial displacements of the reconnection onset site from the observation point ~0.5($R_{obs} - R_{min}$) is then typically only ~6 R_S, such that the onset times differ from the observation times by ~20 min, corresponding to only ~10° of PPO phase. For the few events observed at radial distances less than 25 R_S, we have simply assumed that they are observed very close to the onset site, such that we take $R_{rec} = R_{obs}$ and $T_{rec} = T_{obs}$, the limiting values of equations (3) and (4) when $R_{obs} = R_{min}$.

For the planetward propagating events (Figure 8b) the situation is perhaps less obvious. Here we propose an algorithm based on the assumption that a reconnection event occurring at a certain radial distance downtail produces a detectable dipolarization signature over a distance planetward of the event, which is some fraction $0 \le F \le 1$ of the distance between the reconnection site and some inner radius R_{min}, which we may again take as 25 R_S noting that more than 90% of planetward events are observed outside this distance (see Figure 4d). If this is the case, the maximum radial distance of the reconnection onset site of an event observed at R_{obs} is given by

$$R_{max} = R_{obs} + \left(\frac{F}{1-F}\right)(R_{obs} - R_{min}). \tag{5}$$

Similar to equation (3), we then assume that the actual reconnection site is located planetward of the maximum radial distance at some fraction $0 \le f \le 1$ of the distance between the maximum radial distance given by equation (5) and the observation point

$$R_{rec} = R_{max} - f(R_{max} - R_{obs}) = R_{obs} + (1-f)(R_{max} - R_{obs}), \tag{6}$$

or combining with equation (5), we have

$$R_{rec} = R_{obs} + (1-f)\left(\frac{F}{1-F}\right)(R_{obs} - R_{min}). \tag{7}$$

The onset time of the reconnection event is then

$$T_{rec} = T_{obs} - \left((1-f)\left(\frac{F}{1-F}\right)(R_{obs} - R_{min})/V_{dip}\right), \tag{8}$$

where V_{dip} is the planetward speed of the dipolarization event. This speed is not well documented in literature but may be expected to be comparable with the tailward speed of the related plasmoid disturbance (e.g., Jackman et al. (2015), their section 2.4). Here for commonality with the plasmoid events, we have simply taken a value for V_{dip} of 300 km/s.

As for the tailward propagating events, in section 3 we will examine results for fixed value of f = 0.25, 0.5, and 0.75 in equations (7) and (8), but we also need to estimate the physically determined value of plasma sheet disturbance fraction F. In this regard, we recall from section 2.2 that the number of tailward events exceeds the number of planetward events by a factor close to ~2, a factor that evidently relates to the fraction of the planetward current sheet that is detectably perturbed by dipolarization events. Using the algorithm shown in the appendix, it is clear that if reconnection events are reasonably uniformly distributed with radial distance within the current sheet tailward of R_{min}, then the ratio of the number of planetward propagating dipolarizations to the number of tailward propagating plasmoids at any radial distance down tail is simply given by the constant value $r = F/(1 - F)$. Given the observed ratio of approximately half (e.g.,

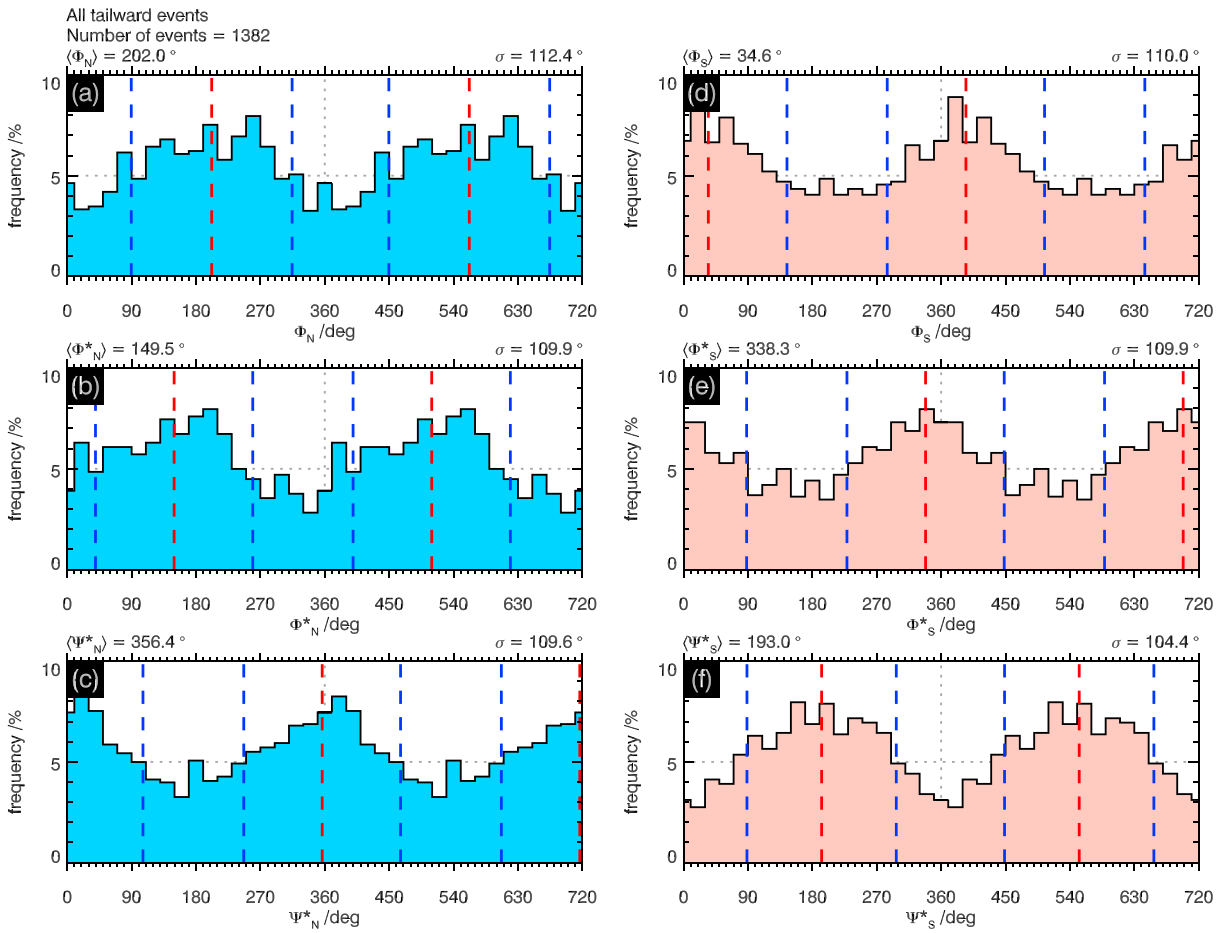

Figure 9. Occurrence frequency histograms of tailward events versus north (Figures 9a–9c) and south (Figures 9d–9f) PPO phases, shown as percentages of the total number of events given in the top left of the figure. Phases are divided into 20° nonoverlapping bins such that no phase modulation would result in a flat profile of ~5.6%. Two cycles of phase are shown on the horizontal axis to aid visualization of the modulo 360° continuity. Vertical red dashed lines show the directional mean phase of the events (equation (9)), while the vertical blue dashed lines show the circular standard deviation range about the means (equation (10)), the values of which are shown to the left and right, respectively, above each panel. The first row (Figures 9a and 9d) shows histograms for the global phases $\Phi_{N,S}$, the second row (Figures 9b and 9e) histograms for the retarded global phases $\Phi^*_{N,S}$, and the third row (Figures 9c and 9f) histograms for the local retarded phases $\Psi^*_{N,S}$.

Figures 4a and 4d), we thus infer $F \approx 1/3$ and put $r = F/(1 - F) = 0.5$ in equations (7) and (8). With median values $R_{obs} \approx 36$ R_S (Figure 4d), the resulting estimated radial displacements of the reconnection onset site from the observation point ~$0.25(R_{obs} - R_{min})$ (for $f \simeq 0.5$) are typically only ~3 R_S, such that the onset times differ from the observation times by ~10 min, corresponding to only ~5° of PPO phase. For those few events that occur with R_{obs} less than R_{min}, we again simply take $R_{rec} = R_{obs}$ and $T_{rec} = T_{obs}$, the limiting values of equations (7) and (8) when $R_{obs} = R_{min}$.

3. Results

3.1. Overall Phase Modulation of Tailward and Planetward Events

We begin with an overall examination of the PPO modulation of the reconnection events in the Smith et al. (2016) data set, encompassing all three event intervals and all event types (e.g., isolated or part of a cluster), but separated into tailward and planetward propagation. Results are shown in Figure 9 for the tailward events and in Figure 10 for the planetward events, where we plot frequency of event occurrence as a percentage of the total number of events in each category versus PPO phase. The phases are divided into 18 nonoverlapping bins of 20° each, such that the absence of modulation would yield a flat profile with ~5.6% of the events in each bin. From Table 1 we note that these plots encompass 1,382 tailward events and 712 planetward events, corresponding to ~77 tailward events and ~40 planetward events per bin.

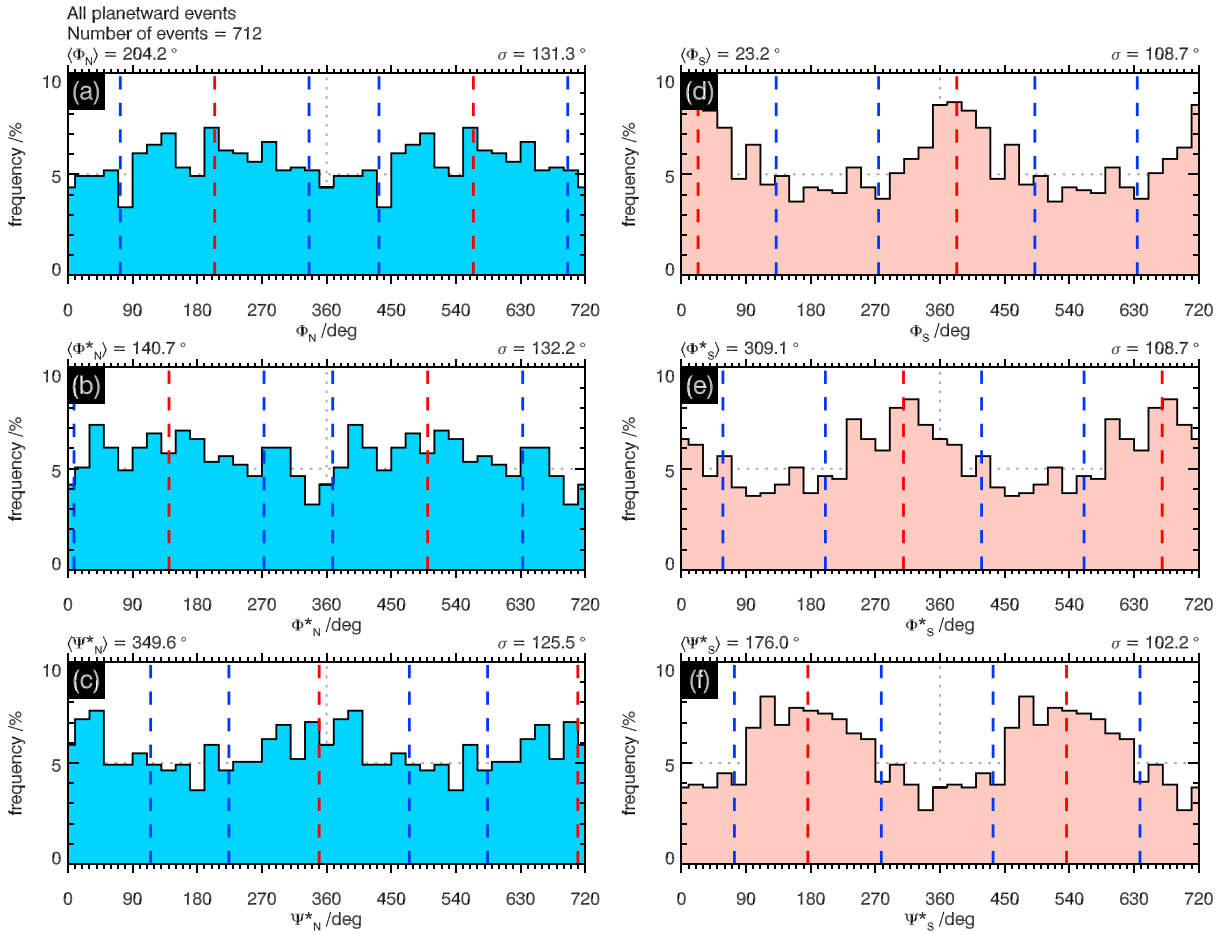

Figure 10. Occurrence frequency histograms of planetward events versus north (Figures 10a–10c) and south (Figures 10d–10f) PPO phases, in the same format as Figure 9.

Figures 9a–9c show results for the tailward events ordered by north system PPO phases, specifically by the value of the north PPO phase at the estimated reconnection time $\Phi_N(T_{rec})$, the retarded phase angle $\Phi^*_N(T_{rec}, R_{rec})$ given by equation (1), and the local retarded phase angle $\Psi^*_N(T_{rec}, R_{rec})$ given by equation (2), respectively. Figures 9d–9f similarly show results for the tailward events ordered by the corresponding south system PPO phases, $\Phi_S(T_{rec})$, $\Phi^*_S(T_{rec}, R_{rec})$, and $\Psi^*_S(T_{rec}, R_{rec})$, respectively. Two cycles of phase are plotted in each panel to aid visualization of the modulo 360° continuity. We have also used $f = 0.5$ in equations (3) and (4) in estimating R_{rec} and T_{rec} from the observed values (we examine sensitivity to this choice in section 3.2).

Similar variations in event frequency are seen with respect to both north and south PPO phases in all panels of Figure 9, demonstrating clear dependence of the Smith et al. (2016) tailward events on both PPO phases, similar to the previous results of Jackman et al. (2016). The red dashed vertical lines in each panel show the value of the *directional mean* of the phase data, essentially marking the phases of the peaks in the modulation, while the blue dashed lines on either side show the *circular standard deviation*, essentially marking the width of the peaks. Following Mardia and Jupp (2000), the directional mean $\langle\psi\rangle$ of a set of K angles ψ_k is given by

$$\frac{1}{K}\sum_{k=1}^{K} e^{i\psi_k} = \mathrm{Re}^{i\langle\psi\rangle}, \tag{9}$$

where pure real modulus R is the mean resultant length of the data and the circular standard deviation is given (in radians) by

Table 2
Variation of Directional Mean Phases and Circular Standard Deviations With f Value for Both Tailward and Planetward Events

Event type	Tailward events			Planetward events		
f	0.25	0.5	0.75	0.25	0.5	0.75
$\langle\Phi_N\rangle$/deg	197.8	202.0	205.9	198.0	201.2	204.2
σ/deg	111.5	112.4	113.4	131.0	131.2	131.3
$\langle\Phi^*_N\rangle$/deg	152.2	149.5	146.7	115.5	128.6	140.7
σ/deg	110.3	109.9	110.0	135.7	133.7	132.2
$\langle\Psi^*_N\rangle$/deg	359.8	356.4	352.9	325.4	337.7	349.6
σ/deg	109.6	109.6	109.6	128.7	126.9	125.5
$\langle\Phi_S\rangle$/deg	29.2	34.6	40.0	14.7	19.0	23.2
σ/deg	109.8	110.0	110.2	108.5	108.6	108.7
$\langle\Phi^*_S\rangle$/deg	341.8	338.3	334.7	284.0	296.6	309.1
σ/deg	109.8	109.9	110.0	110.1	109.3	108.7
$\langle\Psi^*_S\rangle$/deg	196.3	193.0	189.7	150.7	163.3	176.0
σ/deg	103.7	104.4	105.1	106.7	103.8	102.2

$$\sigma = \sqrt{\ln\left(\frac{1}{R^2}\right)}. \tag{10}$$

Note that this value relates to the width of the peaks, not to the accuracy with which the directional mean is determined. Corresponding values are given in Figure 9 at the top of each plot. It can be seen that the tailward event distributions peak at north and south PPO phases $\Phi_{N,S}$ of 202° and 35°, respectively, reducing to 150° and 338°, respectively, for the retarded phases $\Phi^*_{N,S}$. Thus, the retardation results in overall phase delays of ~55°, in accordance with the discussion in section 2.5. This means that, overall, at the start time of these events the $\Psi^*_N = 0°$ meridian of the retarded north PPO system is preferentially located in the premidnight sector at ~22-hr LT, while the $\Psi^*_S = 0°$ meridian of the retarded south PPO system is preferentially located at ~10.5-hr LT in the prenoon sector. As discussed in section 2.5 and illustrated in Figures 5 and 6, these are the phases for which the nightside current sheet is the thinnest specifically in the premidnight sector ~22–23-hr LT, close to the median LT of the Smith et al. (2016) events (Figure 4b). Correspondingly, the events peak at local retarded north and south PPO phases $\Psi^*_{N,S}$ of 356° and 193°, respectively, close to the local phases at which the current sheet should be thinnest with the weakest normal field.

We recall from the discussion in section 2.5 that if the events are more global in nature, we might expect best organization by the retarded phase angles $\Phi^*_{N,S}$, while if more local in nature, then by the local retarded phase angles $\Psi^*_{N,S}$. Although the distributions with respect to $\Phi^*_{N,S}$ and to $\Psi^*_{N,S}$ are quite similar, there is some indication in the profiles in Figure 9 of better organization by the local phases, such as the lower and sharper minimum percentage values for Ψ^*_S in Figure 9f compared with those for Φ^*_S in Figure 9e (or for Φ_S in Figure 9d). The circular standard deviation of each distribution provides a quantitative measure, from which it is seen that the local phases do result in (slightly) smaller values, with occurrence frequency at the peaks near phases $\Psi^*_N \approx 0°/360°$ and $\Psi^*_S \approx 180°$ being a factor of ~3 larger than those at the antiphase points, thus supporting the results of Jackman et al. (2016) concerning the occurrence of tailward propagating plasmoid events.

In Figure 10 we newly show results for planetward propagating dipolarization events in the same format as Figure 9, where for reasons outlined in section 3.2 we have used $f = 0.75$ (and $F/(1 - F) = 0.5$) in equations (7) and (8) for R_{rec} and T_{rec}. PPO-related modulation can again be seen in all panels, similar in nature to the tailward event modulation for the south PPO phases (similar σ values) but weaker for the north PPO phases (larger σ values). Directional mean phases are at similar north and south PPO phases as for the tailward events within ~20°, with the principal global PPO meridians at 204° and 23°, now retarded by ~70° to 141° and 309°, corresponding to maximum thinning in the premidnight sector at ~21-hr LT, again close to the median LT of the Smith et al. (2016) events (Figure 4e). Smallest values of σ are again for local rather than global phases, with occurrence frequency at the peaks being ~3 times that near the antiphase point for the south PPO phase (Figure 10f), similar to the tailward events, but with a smaller factor of ~1.75 for the north PPO phase (Figure 10c). We also note that unlike for the tailward events, retardation of the global phases does not improve the σ values. Local retarded north and south PPO phases have directional means of 350° and 176°, smaller than the corresponding values for tailward events by ~10°–20°, but again corresponding to values close to where the current sheet should be thinnest.

3.2. Effect of Varying *f*

We now investigate the effect on these results of varying fraction *f* appearing in the algorithms to transform observed radial distance and time to reconnection distance and time (equations (2), (3), (7), and (8) and section 2.6). Since the histograms in all cases are essentially similar to those shown in Figures 9 and 10, here we only show in Table 2 the directional mean and circular standard deviation values for the tailward and planetward events for three *f* values in each case, namely, 0.25, 0.5, and 0.75. Examination of the values for the tailward events shows that they are quite insensitive to the choice of *f*, varying typically by less than ~10°. This results from the fact that the algorithmic time displacements and radial displacements of the reconnection

event onsets from the observed values result in changes in event phase in opposite senses, such that they tend to cancel. For example, smaller values of *f*, meaning that the reconnection event is assumed to occur closer to R_{min} (Figure 8a), result in earlier event times and hence earlier phases, while the smaller event radius results in a lesser phase retardation and hence later phases. This means that the results for the tailward events are almost independent of *f*, such that we simply choose the central value $f = 0.5$.

For the planetward events, however, the results depend more significantly on *f* value, by typically ~25° for the retarded phases, resulting from the fact that the variations in the algorithmic event times and radial distances produce effects having the same sense as each other. Now smaller values of *f*, meaning that the event is assumed to occur closer to R_{max} (Figure 8b), again result in earlier event times and hence earlier phases, while the larger event radius results in a larger phase retardation and hence also in earlier phases. Examining the values for planetward events in Table 2, it can be seen that the σ values for the retarded phases $\Phi^*_{N,S}$ are increasingly larger than the unretarded phases $\Phi_{N,S}$ for smaller values of *f,* opposite to expectation, but are at least comparable for $f = 0.75$. In addition, the smallest values of σ in the table for these events correspond to the local retarded phases $\Psi^*_{N,S}$ for this value of *f*, hence its adoption in Figure 9, and in subsequent analysis of the planetward events presented below.

3.3. Phase Variation With LT

That the events are best ordered by the local phases $\Psi^*_{N,S}$ (i.e., lowest σ values) suggests that their timing is ordered by LT as the preferred PPO phases sweep around the nightside. To examine whether this is the case, we have divided the *all event* tailward and planetward data into nonoverlapping 1-hr bins of LT over the range 18 to 04 hr via midnight (see Figures 4b and 4e) and have repeated the analysis illustrated in Figures 9 and 10. Results are shown for tailward and planetward events in Figures 11 and 12, respectively, where we plot the directional mean phases and circular standard deviations of the distributions versus LT across the nightside hours. Phases are plotted over two cycles on the vertical axis to allow better visualization of data continuity, with each data point being plotted twice.

Considering first the tailward event results in Figure 11, it can be seen that the mean global phases $\langle\Phi_N\rangle$ and $\langle\Phi_S\rangle$ indeed both generally increase with LT over the range of data from ~150° to ~290° for $\langle\Phi_N\rangle$ in Figure 11a and from ~330° to ~450° (i.e., ~90° modulo 360°) for $\langle\Phi_S\rangle$ in Figure 11d. That is, the phases increase by ~135° over the range, corresponding to ~9-hr LT, effectively the LT range of the data between 18.5 and 3.5 hr via midnight. The mean retarded global phases correspondingly increase over similar ranges from ~90° to ~210° for $\langle\Phi^*_N\rangle$ in Figure 11b and over ~270° to ~400° (i.e., ~40° modulo 360°) for $\langle\Phi^*_S\rangle$ in Figure 11e. However, when account is taken of the LT (i.e., the longitude) of the data as in the local phases $\langle\Psi^*_{N,S}\rangle$ given by equation (2), then the rising nature of the phase data is seen to be essentially eliminated in Figures 11c and 11f, with near-constant values generally just less than ~360° for $\langle\Psi^*_N\rangle$ in Figure 11c and generally just greater than ~180° for $\langle\Psi^*_S\rangle$ in Figure 11f, in agreement with the results shown in Figures 9c and 9f and Table 2. These results thus clearly indicate that the tailward events are essentially local in nature, tending to occur with increasing time as the preferred PPO phases rotate across the nightside. We note that azimuthal localization of tail reconnection events has also been inferred by Smith, Jackman, Thomsen, Sergis, et al. (2018) on the basis of short-lived intervals of tailward flow observed during an individual event study.

Corresponding plots for the planetward events in Figure 12 show similar features, though with greater data scatter due to the smaller number of events and with some modulo 360° ambiguity in the LT behavior of the weaker modulations with the global and global retarded northern phases. Again, however, the local retarded phases achieve relatively constant values of typically a little less than ~360° for $\langle\Psi^*_N\rangle$ in Figure 12c, and a little less than ~180° for $\langle\Psi^*_S\rangle$ in Figure 12f, in agreement with the results in Figures 10c and 10f and Table 2. The results in Figures 11 and 12 thus show that overall these events are best organized by the local retarded phases $\Psi^*_{N,S}$, so we will concentrate on these in the remainder of this study.

3.4. Modulation of Isolated and Clustered Events

The analysis in sections 3.1–3.3 examined the PPO modulations of the reconnection event data set overall, separated only into tailward and planetward events, while now we consider the modulations of individual event types, that is, isolated events separated from others by more than 3 hr, primary events that begin a

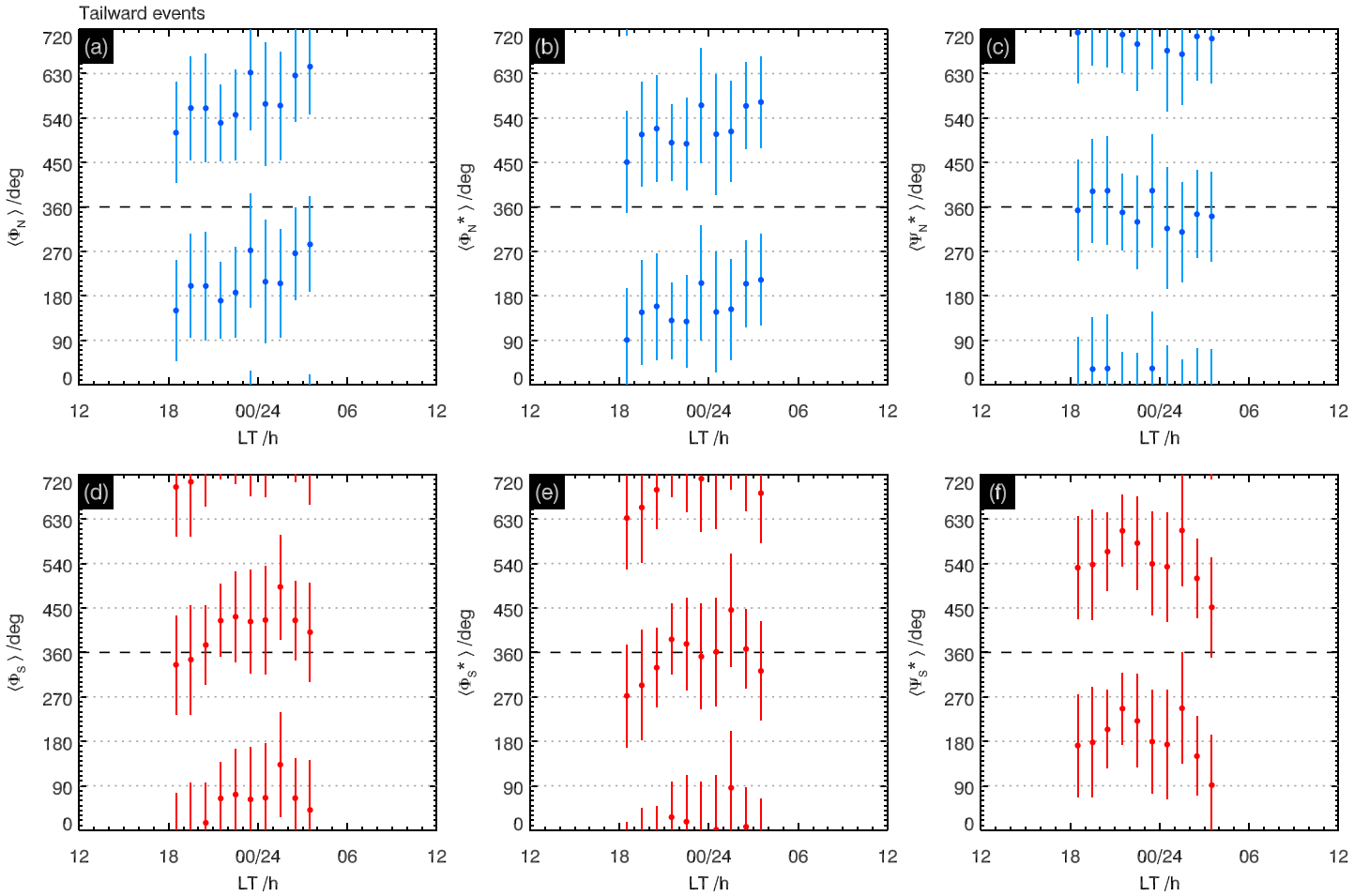

Figure 11. Plots showing the directional mean phases (colored circles) and circular standard deviations (colored lines) versus LT for tailward event data divided into 1-hr nonoverlapping LT bins centered every half hour between 18.5 and 3.5 hr via midnight. Two cycles of phase are shown on the vertical axes with each data point being plotted twice. Figures 11a–11c and 11d–11f show results for the northern (blue) and southern (red) phases, respectively, where from left to right the panels show the mean global phases $\langle \Phi_{N,S} \rangle$, the mean retarded global phases $\left\langle \Phi^*_{N,S} \right\rangle$, and the mean local retarded phases $\left\langle \Psi^*_{N,S} \right\rangle$.

cluster of events with members separated by 3 hr or less, and the secondary subsequent cluster events (Table 1). Because their numbers are relatively small, results for the isolated events individually are rather noisy, but within the limitations thereby imposed are found in initial examination not to differ significantly from those of the primary cluster events. Here we therefore take the isolated plus primary cluster events as a single group related to the start of independent reconnection episodes and consider them separately from the secondary cluster events. Table 1 shows that for both tailward and planetward events the number of secondary events is larger than that of isolated plus primary cluster events by a factor of ~2.5, so that the modulation properties of the event data set taken overall as shown in Figures 9 and 10 are expected to be related more specifically to the secondary events than to the isolated plus primary.

That this is indeed the case is shown in Figure 13, where we plot local retarded phase frequency histograms in a similar format to Figures 9 and 10 for both tailward (Figures 13a–13d) and planetward (Figures 13e–13h) events for the data set as a whole but now split into isolated plus primary cluster events (Figures 13a and 13b and 13e and 13f) and secondary cluster events (Figures 13c and 13d and Figures 13g and 13h). We note the change in percentage frequency scale on the vertical axes, chosen for commonality with related Figures 14–16 introduced below. It can be seen that for both tailward and planetward events the frequency of secondary cluster events peaks at values close to ~360° for the northern local retarded phase Ψ^*_N, as for the overall data set in Figures 9c and 10c, and at values close to ~180° for the southern retarded local phase Ψ^*_S, as for the overall data set in Figures 9f and 10f, these being the phases at which the current sheet is expected to

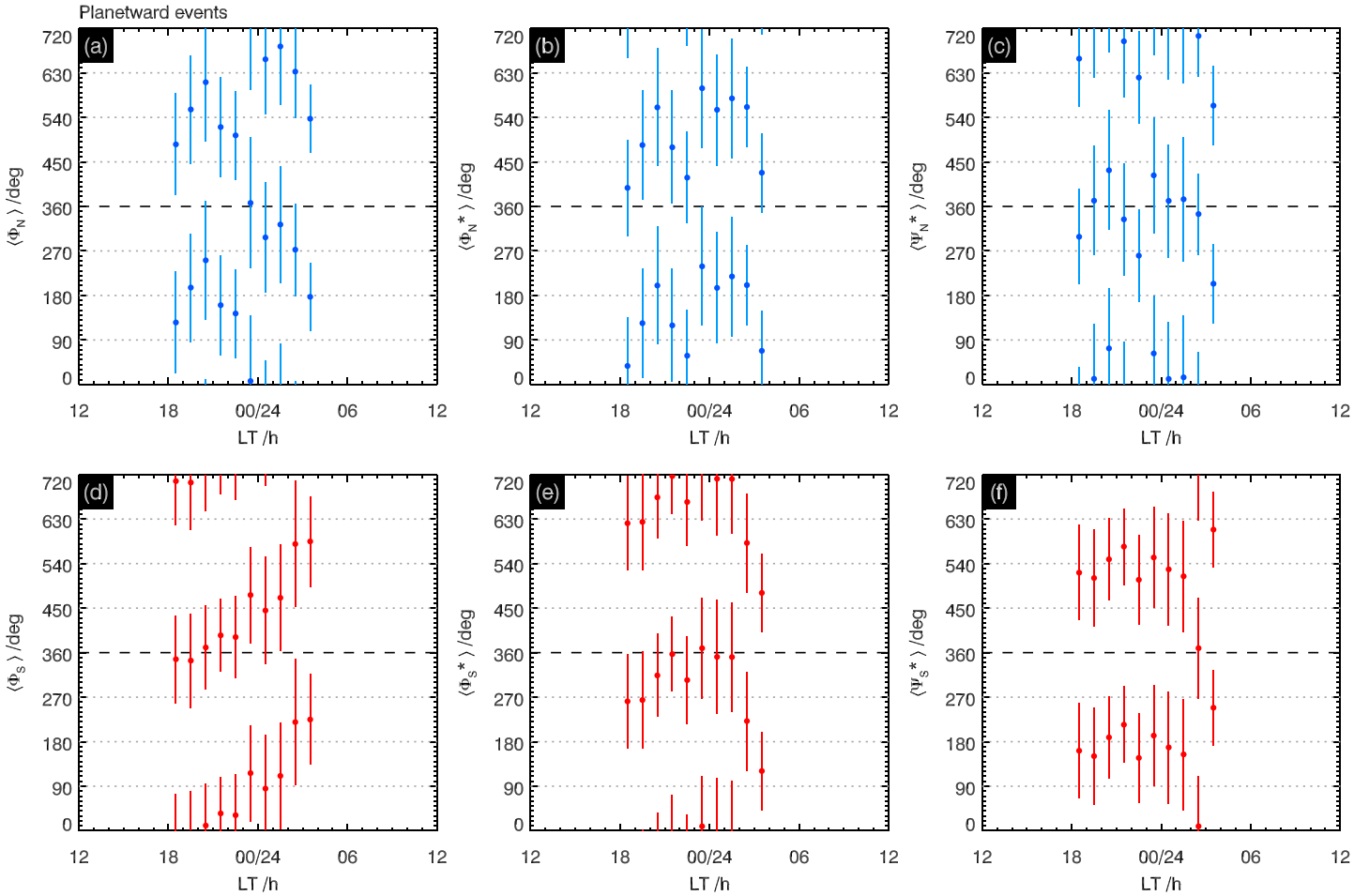

Figure 12. Plots showing the directional mean phases and circular standard deviations versus LT for planetward event data divided into 1-hr nonoverlapping LT bins centered every half hour between 18.5 and 3.5 hr via midnight, in the same format as Figure 11.

be the thinnest (Figure 6). However, as might then be expected from the temporal sequences involved, the frequency of isolated plus primary cluster events peaks at somewhat earlier phases, typically by ~60°, with frequencies peaking at northern local retarded phases of ~320° in Figures 13a and 13e, and at southern local retarded phases of ~120° in Figures 13b and 13f.

As can be seen in Figure 6, these correspond to phases for which the plasma and field lines of the thinning plasma sheet are also displaced outward from the planet. For easy reference, directional mean phase values and circular standard deviations are recorded in the all intervals section of Table 3. The phase displacement between the secondary events and the isolated plus primary events is evidently related principally to the displacement in time between primary cluster events and subsequent secondary events. For the data set as a whole, and taking tailward and planetward events together, the mean time displacement is found to be ~3 hr, with a ~70° directional mean PPO phase shift, close to the phase differences indicated above.

3.5. Results for Individual Temporal Intervals

In Figures 14–16 we show local retarded phase modulation results for the isolated plus primary and secondary cluster events in the same format as Figure 13 but now separately for the three temporal intervals discussed in section 2.1, namely, the 2006 equatorial orbit data, the 2006 inclined orbit data, and the 2009/2010 near-equatorial data, respectively (see Figures 1 and 2). Values are again recorded for easy reference in Table 3. The results from each interval are seen generally to be similar to each other and to the overall results in Figure 13, especially for the 2009/2010 data in Figure 16 that provides close to half of the event data set (Table 1). Specifically, the isolated plus primary cluster events generally peak at northern phases between

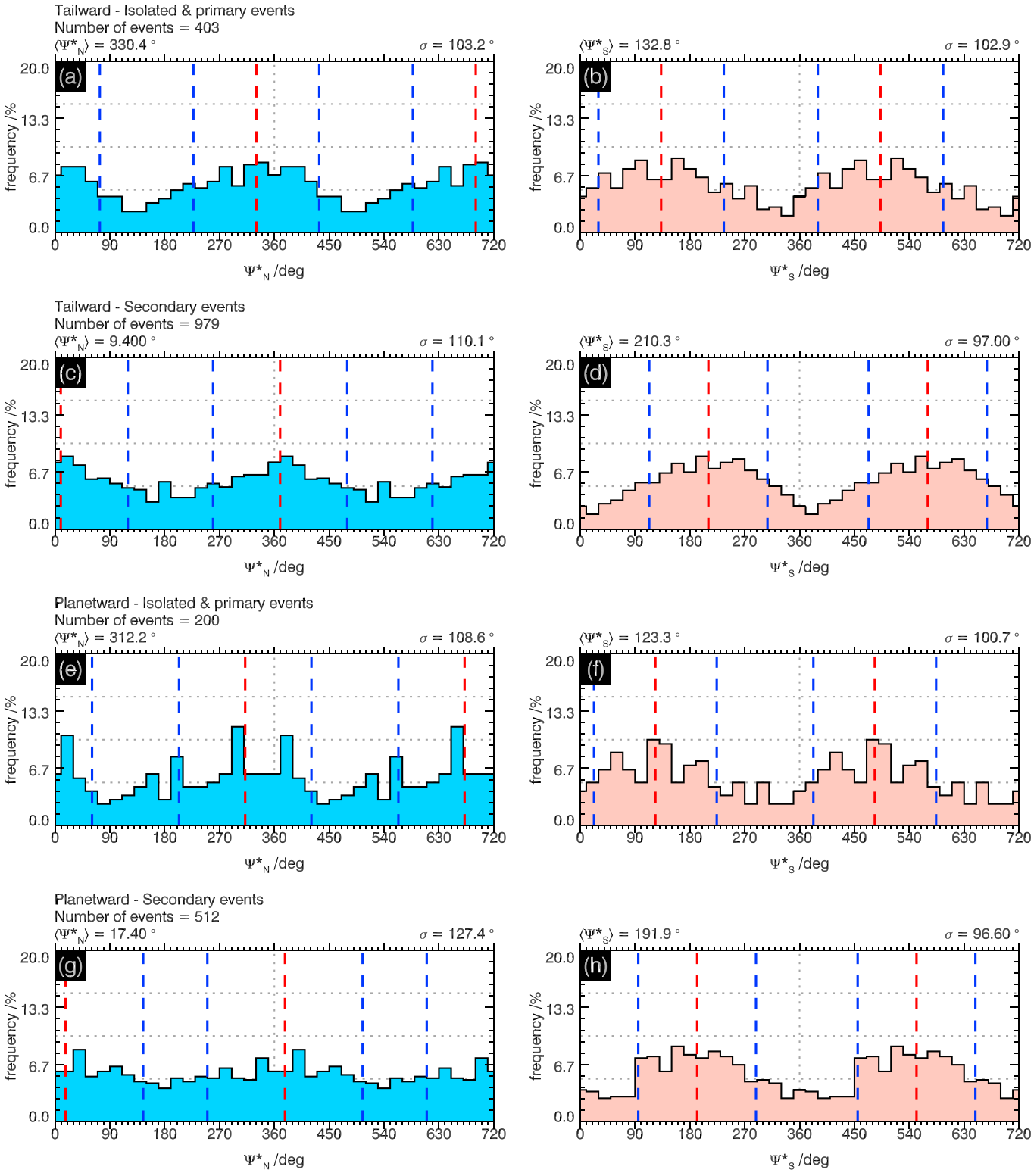

Figure 13. Occurrence frequency histograms versus retarded local phases $\Psi^*_{N,S}$ for both tailward (Figures 13a–13d) and planetward (Figures 13e–13h) events, in a similar format to Figures 9 and 10, but separating the event data into isolated plus primary cluster events (Figures 13a and 13b and 13e and 13f) and secondary cluster events (Figures 13c and 13d and 13g and 13h). Note the change in frequency scale compared with Figures 9 and 10, chosen for commonality with Figures 14–16.

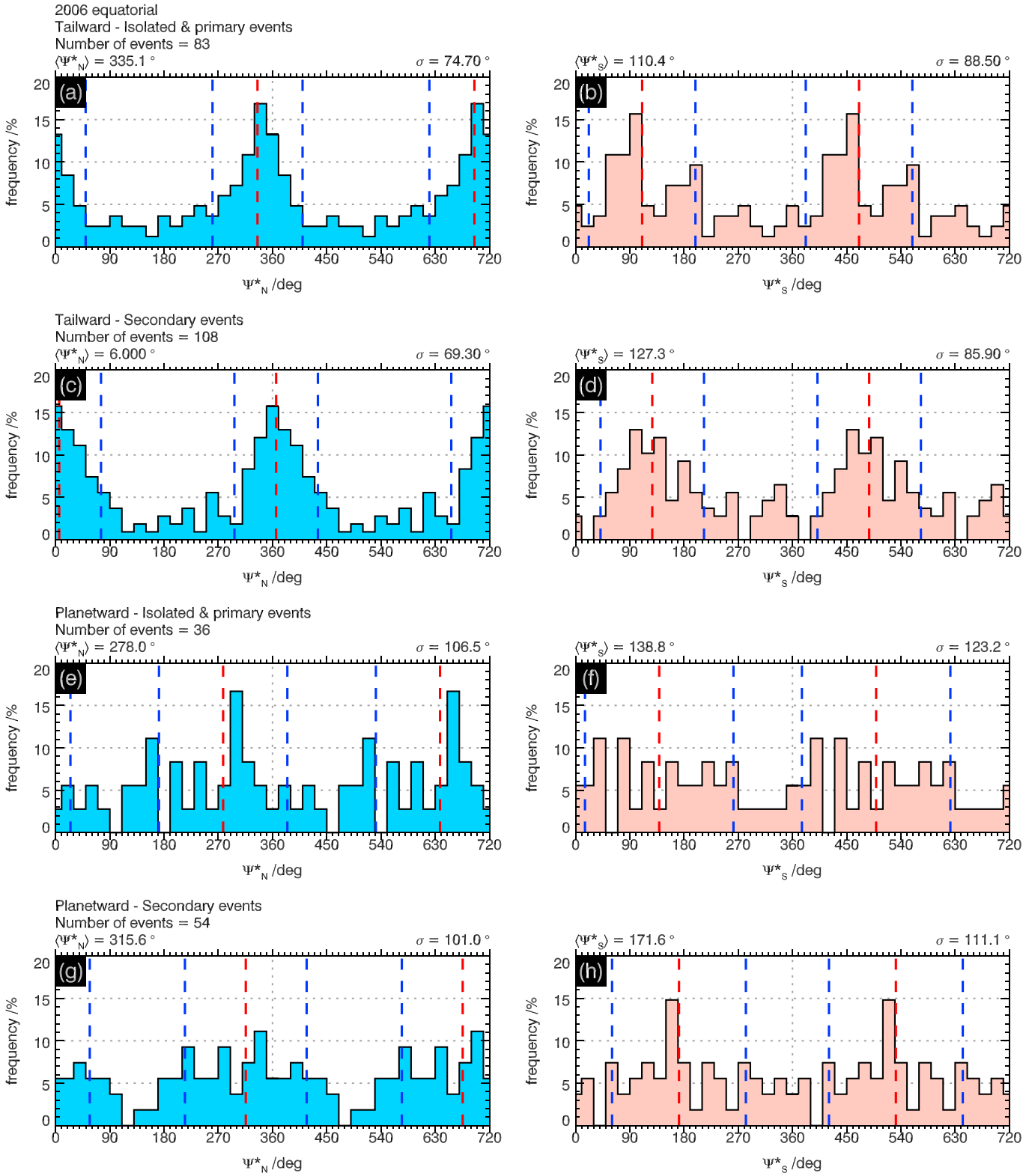

Figure 14. Occurrence frequency (percentage of events) histograms versus local retarded phases for tailward and planetward isolated plus primary and secondary cluster events, in the same format as Figure 13 but for the 2006 equatorial orbit interval only.

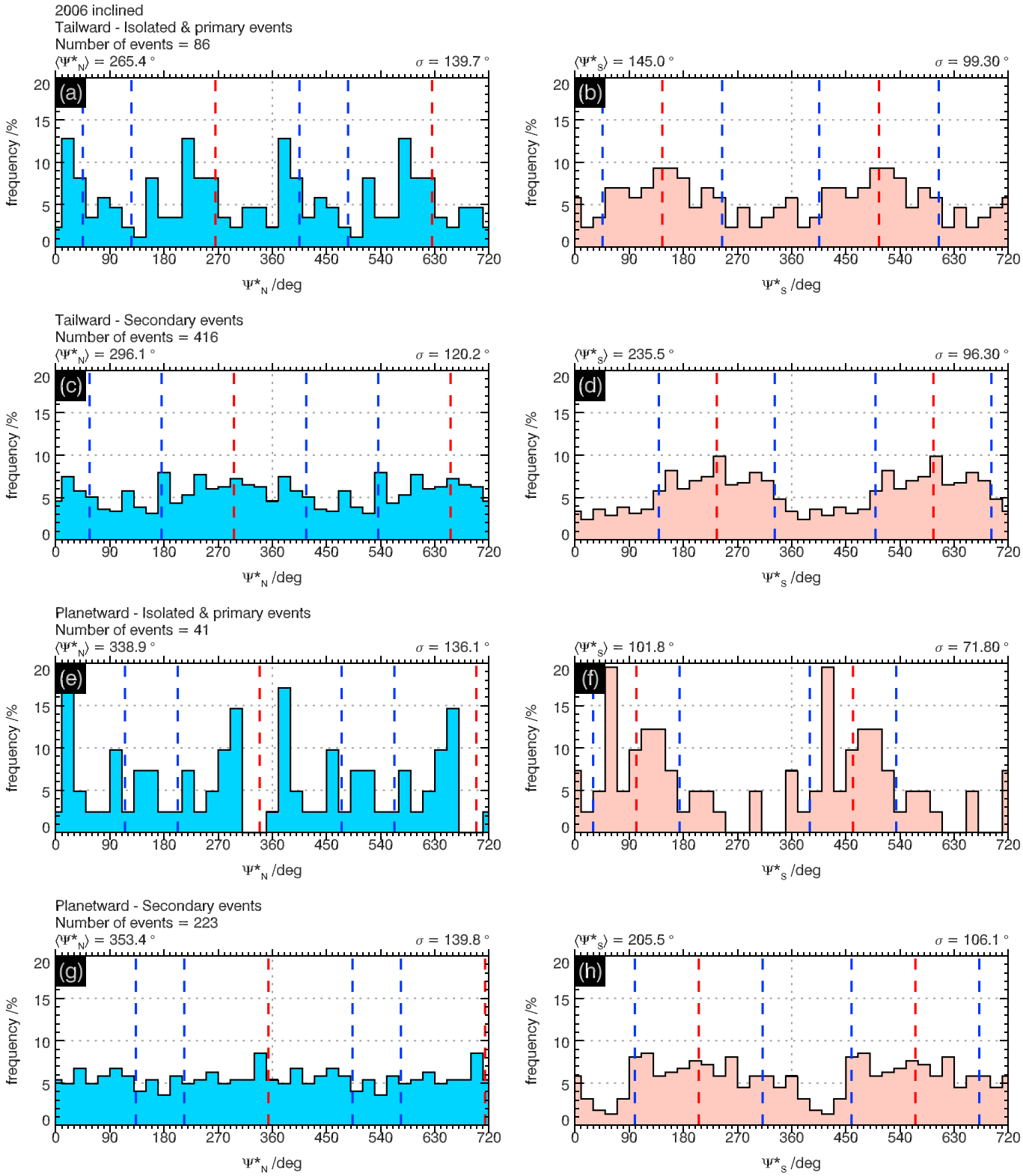

Figure 15. Occurrence frequency histograms versus local retarded phases for tailward and planetward isolated plus primary and secondary cluster events, in the same format as Figure 14, but for the 2006 inclined interval events.

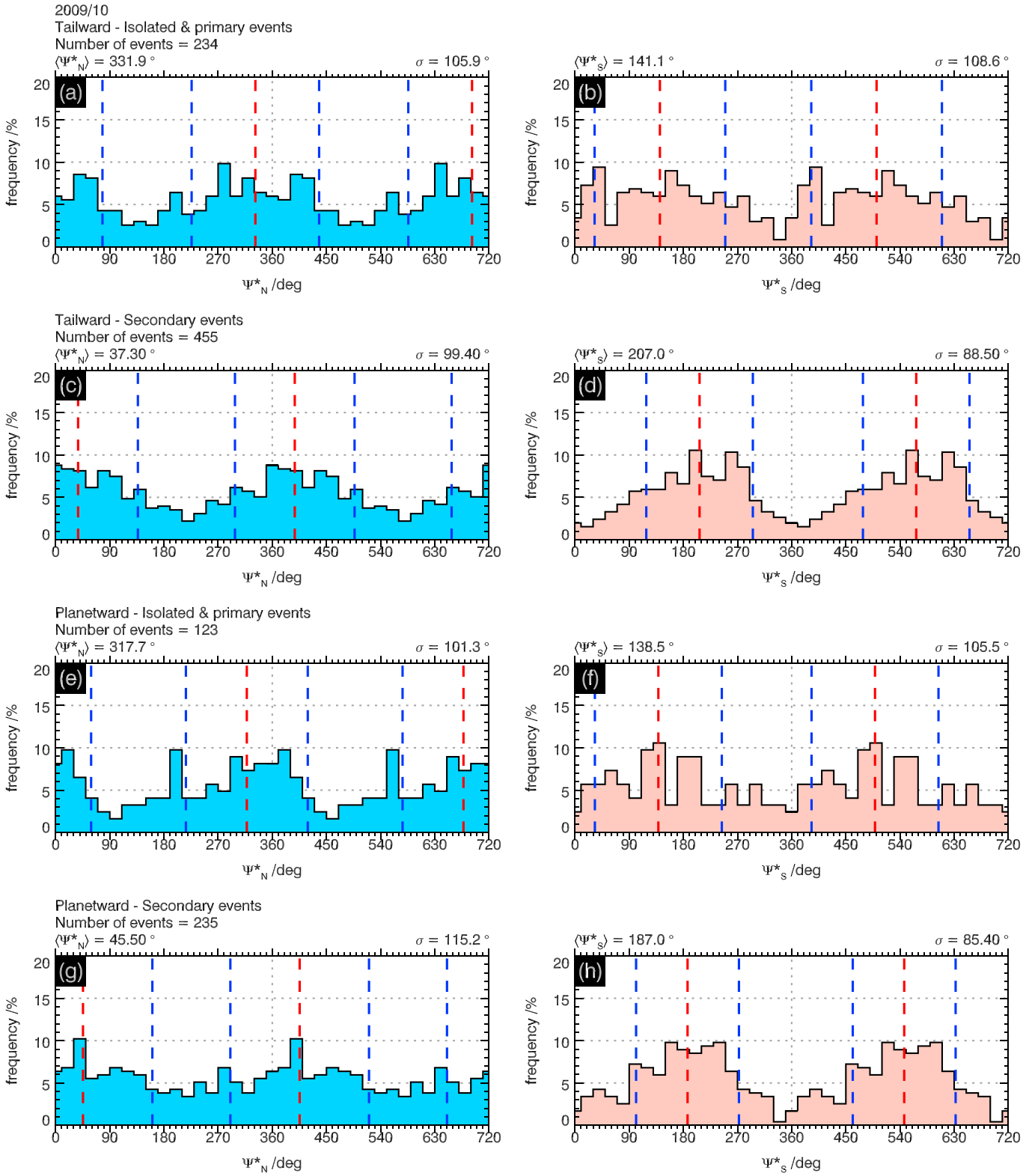

Figure 16. Occurrence frequency histograms versus local retarded phases for tailward and planetward isolated plus primary and secondary cluster events, in the same format as Figures 14 and 15, but for the 2009/10 events.

Table 3
Directional Mean Phases and Circular Standard Deviations of Maximum Event Occurrence Frequency for Tailward and Planetward Events, Separated by Event Interval and Event Type

	Tailward events		Planetward events	
Event type	Isolated and primary cluster	Secondary cluster	Isolated and primary cluster	Secondary cluster
2006 equatorial orbit interval				
$\langle\Psi_N^*\rangle$/deg	335.1	6.0	278.0	315.6
σ/deg	74.7	69.3	106.5	101.0
$\langle\Psi_S^*\rangle$/deg	110.4	127.3	138.8	171.6
σ/deg	88.5	85.9	123.2	111.1
2006 inclined orbit interval				
$\langle\Psi_N^*\rangle$/deg	265.4	296.1	338.9	353.4
σ/deg	139.7	120.2	136.1	139.8
$\langle\Psi_S^*\rangle$/deg	145.0	235.5	101.8	205.5
σ/deg	99.3	96.3	71.8	106.1
2009/2010 interval				
$\langle\Psi_N^*\rangle$/deg	331.9	37.3	317.7	45.5
σ/deg	105.9	99.4	101.3	115.2
$\langle\Psi_S^*\rangle$/deg	141.1	207.0	138.5	187.0
σ/deg	108.6	88.5	105.5	85.4
All intervals combined				
$\langle\Psi_N^*\rangle$/deg	330.4	9.4	312.2	17.4
σ/deg	103.2	110.1	108.6	127.4
$\langle\Psi_S^*\rangle$/deg	132.8	210.3	123.3	191.9
σ/deg	102.9	97.0	100.7	96.6

~270° and ~360° and southern phases between ~90° and ~180° associated with outward radial field displacements and thinning current sheets, while the secondary events generally peak at phases that are later by some tens of degrees, closer to maximally thinned current sheet conditions. In this regard, we note from the values in Table 3 that the differences in directional mean phases between the isolated plus primary events and the secondary events in a given temporal interval that are reasonably well determined, ~35° for the 2006 equatorial orbit interval, ~90° for the 2006 inclined orbit interval, and ~65° for the 2009/2010 interval, vary roughly in concert with the mean number of secondary events in clusters, as might be expected.

In somewhat more detail, it can first be seen in Figure 16 for the 2009/2010 near-equatorial orbit data, when the spacecraft was located generally near the center of the current sheet (Figure 3b), that the events are similarly modulated by both northern and southern PPO systems. Such behavior is consistent with the two PPO systems having closely similar amplitudes during this interval as shown in Figure 7d (north/south amplitude ratio $k \approx 1.01$). For the 2006 inclined orbit data in Figure 15 when the spacecraft was also located generally close to the current sheet (Figure 3b), modulation by the southern system is comparable to that during 2009/2010, consistent with similar southern system amplitudes during the two intervals (Figure 7c). However, the northern PPO modulation during the 2006 inclined orbit interval is much weaker, reflecting the weaker northern PPO amplitude during that interval ($k \approx 0.38$; see Figure 7d).

For the 2006 equatorial orbit data in Figure 14 under similar PPO conditions, but when the spacecraft was generally located well south of the seasonally displaced current sheet (Figure 3b), we find not only a similar modulation by the dominant southern PPO system as may be expected but also an unexpectedly large modulation by the weaker northern PPO system, with event frequencies peaking strongly near ~0°/360° for tailward events in Figures 14a and 14c and a few tens of degrees earlier for planetward events in Figures 14e and 14g. Similar results were found for tailward events in this interval by Jackman et al. (2016), though based on a significantly smaller event data set. A possible explanation for this strong northern system modulation is contained in Figures 4 and 6. As we have seen, events generally cluster in phase in the center of the plot where Ψ_N~0°/360° and Ψ_S~180° such that the current sheet is expected to be thin. However, this is also the condition under which the dominant southern system displaces the current sheet north of its

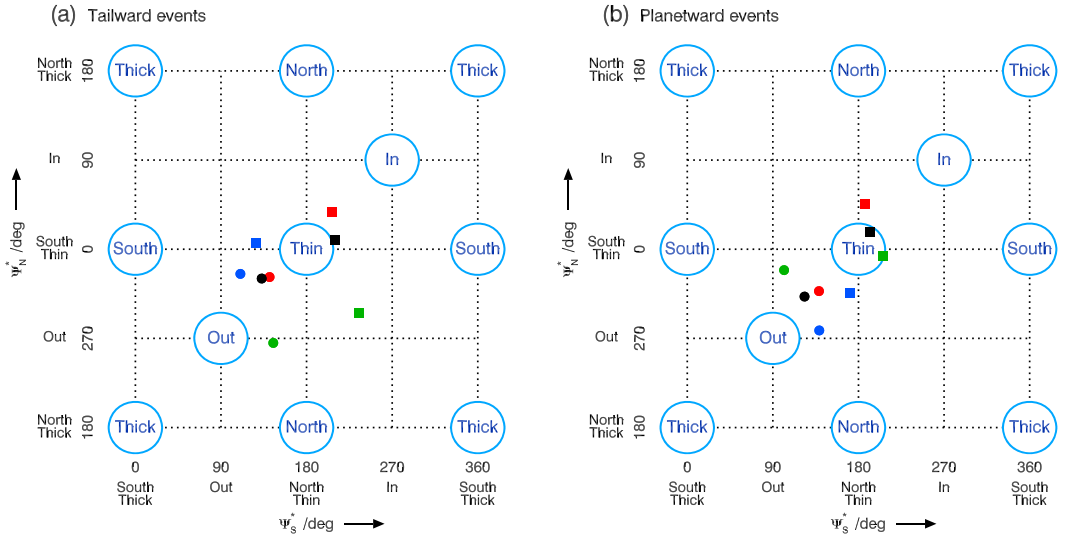

Figure 17. The directional means of the isolated and primary cluster events (circles) and the secondary cluster events (squares) are shown plotted on the $\Psi_N^* - \Psi_S^*$ local retarded phase plane, following the format of Figure 6. Blue symbols correspond to the 2006 equatorial orbit interval (Figure 14), green to the 2006 inclined orbit interval (Figure 15), red to the 2009/2010 interval (Figure 16), and black to the overall data set (Figure 13).

equilibrium position, yet further away from the equatorial spacecraft (Figure 3b), thus opposing detection of the reconnection-related field perturbations. At northern phases of ~0°/360° the current sheet is displaced southward toward the spacecraft reducing this effect and apparently then making the events potentially detectable, which they evidently generally are not at ~180° northern PPO phases. We thus suggest that this particular feature is possibly attributable to an event *seeing* effect, rather than to an event occurrence effect. From Table 1 we note that the overall event frequency during the 2006 equatorial orbit interval is about half that of the other two intervals and that the mean number of events observed in a cluster is also about half that for the adjacent 2006 inclined orbit interval for which PPO conditions were similar, 3.4 events per cluster, including the primary event, compared with 7.1. We also note from Figure 3b that a net northward deflection of the current sheet by a few Saturn radii during the thin phase will not be a major issue with regard to seeing during the 2006 inclined orbit interval and that the two north-south displacement effects should essentially cancel under this condition during the 2009/2010 near-equatorial orbit interval when the two PPO systems are of comparable amplitude.

Overall, phase results are summarized in Figure 17, where we plot the directional mean phases on the $\Psi_N^* - \Psi_S^*$ phase plane following Figure 6, for the tailward events in Figure 17a and for the planetward events in Figure 17b. The black circles show the directional mean phases of the isolated plus primary cluster events over all intervals as shown in Figures 13a and 13b for the tailward events and Figures 13e and 13f for the planetward events, while the black squares show the mean phases of the secondary cluster events as shown in Figures 13c and 13d for the tailward events, and Figures 13c and 13d for the planetward events. The corresponding directional means for the individual temporal intervals from Figures 14–16 are also similarly shown, blue for the 2006 equatorial interval, green for the 2006 inclined interval, and red for the 2009/2010 interval (see also Table 3). It can be seen that the values for the 2009/2010 interval (red) are similar to the overall results (black), as may be expected since they contribute half the event data, with the mean phases for the isolated plus primary cluster events being located near northern phases ~315° and southern phases ~135° approximately midway between phases where the two systems maximally displace field lines away from the planet and those where the current sheet is thinnest. The mean secondary cluster event phases more favor the latter condition. For the 2006 event data the directional mean phases of the isolated plus primary events are quite closely similar for the dominant southern system phases but are somewhat more broadly distributed in the range ~270° to 0°/360° for the weaker northern system phases. The displacements in phase of the secondary cluster events compared with the isolated plus primary events are also seen to be in rough concert with the mean number of secondary events in a cluster (Table 1), as mentioned above.

4. Summary and Conclusions

As discussed in section 1, previous studies using in situ magnetic field and plasma data and remote sensing observations of ENA, auroral UV, and radio emissions have shown that dynamical events in Saturn's magnetosphere are ordered on semirecurrent timescales near the planetary (PPO) rotation period and also less frequently but more powerfully on the solar rotation time scale, the latter events being associated with strong CME/CIR-related magnetospheric compressions by the solar wind. Both types of dynamical event are associated with hot plasma injections from the tail and associated auroral phenomena that propagate from the nightside to the dayside via dawn and are thus believed to be caused by reconnection events in the tail. However, the frequent semirecurrent events typically do not involve significant closure of open tail flux and are thus associated principally with the Vasyliunas cycle, while major open flux closure occurs during the less frequent CME/CIR-related events, which thus also involve the Dungey cycle. Following initial studies by Jackman et al. (2009, 2016) of modest samples of plasmoid events observed in Saturn's tail, in this paper we have examined the PPO dependence of a large catalogue of 2,094 reconnection-related events, including both tailward propagating plasmoids and planetward propagating dipolarizations, recognized principally via bipolar perturbations in the colatitudinal field component directed approximately perpendicular to the tail current sheet. As also discussed in section 1, PPO modulation of tail reconnection events may be anticipated from previous studies that have demonstrated strong PPO modulations of tail plasma/current sheet properties, not only periodic north-south displacements but also thickening and thinning associated with modulations of the colatitudinal field, as well as radial displacements of the plasma and flux tubes during the northern and southern PPO cycles, which may be expected to strongly affect current sheet stability. Our principal findings are as follows.

1. Using the order of magnitude larger data set of tailward events provided by the Smith et al. (2016) catalogue, we confirm the previous results of Jackman et al. (2016) that the occurrence of plasmoid events in Saturn's tail is significantly modulated at the PPO periods. Overall, events occur more frequently by factors of ~3 at local retarded PPO phases $\Psi^*_N \approx 0°/360°$ and $\Psi^*_S \approx 180°$ compared with the antiphase conditions. The phases of maximum plasmoid occurrence are those for which we expect the thinnest current sheet threaded by the weakest colatitudinal field, conducive to current sheet instability and reconnection.
2. Planetward propagating dipolarization events in Saturn's tail, less frequent in the Smith et al. (2016) catalogue than tailward propagating plasmoids by a factor of ~2, have been shown for the first time to be correspondingly modulated at similar PPO phases, though with a reduced overall modulation ratio with respect to the northern PPO phase.
3. The reconnection events have been shown to be better organized by the local retarded PPO phases $\Psi^*_{N,S}$ that take account of the local time of the events, than by the global retarded PPO phases $\Phi^*_{N,S}$, indicating that the events are localized in azimuth across the tail rather than being more tail-wide in nature. The modulation in event occurrence frequency thus propagates with the local PPO phases across the tail from dusk to dawn as the PPO systems rotate. This finding also implies that the number of reconnection episodes occurring in the tail is larger than that implied by the numbers observed at the spacecraft, roughly by the inverse ratio of the undetermined fraction of the tail width sensibly perturbed by a given event.
4. Dividing the events into three types, namely, isolated (from others by at least 3 hr) events ~10%, primary cluster (start of cluster sequence) events ~20%, and secondary cluster (subsequent cluster sequence) events ~70%, shows that the modulation phasing indicated above is specifically characteristic of the majority secondary cluster events. Isolated plus primary cluster events are found to have similar modulation behavior (within limitations imposed by the smaller number of these events), but with occurrence frequency peaking somewhat earlier in phase than for secondary cluster events, at $\Psi^*_N \approx 315°$ for the northern phase and at $\Psi^*_S \approx 135°$ for the southern phase. These phases are those for which the current sheet is moving toward its minimum thickness configuration with the tail field lines moving inward from their maximum outward radial distension in the PPO cycle.
5. Dividing the events into temporal intervals comprising the 2006 equatorial orbit interval ~15%, the 2006 inclined orbit interval ~35%, and the 2009/2010 near-equatorial orbit interval ~50%, shows related modulations for all intervals. The 2009/2010 events, similar to the all-interval results summarized above, are near-equally modulated by both northern PPO and southern PPO systems with peak-to-trough occurrence frequency ratios ~3, while the 2006 inclined orbit events are similarly modulated by the southern PPO system but less modulated by the northern PPO system, with a peak-to-trough

occurrence frequency ratio of ~2. This behavior is taken to relate to the corresponding behavior of the PPO amplitudes, which are near equal during the post equinox 2009/2010 interval, while during the pre-equinox 2006 intervals the southern PPO amplitude is marginally higher than during 2009/2010, but the northern PPO amplitude is considerably lower.

6. Contrarily, while events continue to be strongly modulated by the southern PPO system during the 2006 equatorial orbit interval, these events also show the strongest modulation by the northern PPO system, with a peak-to-trough occurrence frequency ratio of ~16. We suggest that this results from a seeing effect in which the northern PPO system opposes the northward deflection of the current sheet away from the spacecraft, which accompanies the thinning of the sheet for the dominant southern PPO system. Correspondingly, the event frequency and the number of events per cluster are smaller for the 2006 equatorial orbit interval than for the other intervals. The relative number of events in a cluster also modulates the mean phase separation between the isolated plus primary cluster events and the secondary cluster events, thus being smallest for the 2006 equatorial orbit interval (~3.5 events per cluster) and largest for the 2006 inclined orbit interval (~7 events per cluster).

Overall, these results provide significant support for the large scale picture of Saturn's magnetospheric dynamics outlined in section 1 of this paper. While major disturbances are generated by strong compressions of the magnetosphere by the solar wind, thus recurring on ~25-day solar rotation time scales or some fraction thereof, and typically lasting for a few days, by far the more numerous of Saturn's dynamic events are semi-recurrent on the planetary rotation time scale, lasting for a few hours. Both types of event are associated with tail reconnection, resulting in the injection of hot plasma into the outer nightside magnetosphere followed by convection via dawn around the planet, together with related auroral UV and SKR intensifications. However, whereas the solar wind related events are associated with significant closure of open flux in the tail as part of the Dungey cycle, the planetary periodic events generally are not, instead being primarily associated with the pinch-off of closed loop plasmoids from the tail plasma sheet and the loss of Enceladus plasma as part of the Vasyliunas cycle. In situ studies have shown that the plasma sheet in Saturn's tail is strongly modulated by the magnetospheric PPO perturbations driven from the two polar ionospheres in such a way that its stability to reconnection may be significantly affected, thus providing a potential mechanism for driving magnetospheric dynamics at the planetary (PPO) period. This being the case, we may expect that the signatures of tail reconnection events, specifically of tailward propagating plasmoids and planetward propagating dipolarizations, should be significantly organized by the phases of the ubiquitous PPO perturbations. The analysis presented in this paper of a large catalogue of such events shows that this is indeed the case, with events occurring most frequently at PPO phases associated with thinned plasma sheets threaded by weak radially distended magnetic field lines, conditions likely conducive to the occurrence of reconnection.

Appendix A: Ratio of Planetward to Tailward Reconnection Events

In this appendix we consider the ratio of observed tailward and planetward propagating events, that is, plasmoids and dipolarizations, which result from the simple propagation picture introduced in section 2.6. We assume that over the region of the near-planet tail relevant to the observations, reconnection events occur approximately uniformly with radial distance beyond a minimum value R_{min}, taken on the basis of the results in Figure 4 to be ~25 R_S. We further assume that at a certain observation distance $R_{obs} \geq R_{min}$, all reconnection events encompassing the observation longitude that occur planetward of R_{obs} produce observable tailward propagating plasmoids at that point, while reconnection events encompassing the observation longitude that occur tailward of R_{obs} produce observable dipolarizations at that point only if they occur within a certain maximum radial distance R_{max}. Then for uniform event occurrence with radial distance between R_{min} and R_{max}, the planetward/tailward event ratio r at R_{obs} will be given by the radial distance ratio

$$r = \frac{(R_{max} - R_{obs})}{(R_{obs} - R_{min})}. \tag{A1}$$

If, as in section 2.6, we assume that a reconnection event occurring at a certain radial distance R_{rec} will produce a detectable dipolarization signature only over a distance planetward of R_{rec} that is a fraction F of the

distance between R_{rec} and R_{min}, then R_{max} at a given observation point R_{obs} is given by equation (5). Substitution of this equation into the right side of equation (A1) then yields

$$r = \frac{F}{(1-F)}, \tag{A2}$$

as indicated in section 2.6, that is, a fixed ratio of planetward to tailward events independent of observer position (beyond R_{min}), which may take any positive value between zero for $F = 0$ to infinity for $F = 1$. The observed ratio $r \approx 0.5$ then indicates that $F \approx 1/3$, as indicated in section 2.6.

Acknowledgments
Work at Leicester was supported by STFC Consolidated Grant ST/N000749/1. T. J. B. was supported by STFC Quota Studentship ST/N504117/1 and E. J. B. by a Royal Society Wolfson Research Merit Award. A. W. S. was funded by a SEPnet PhD studentship and C. M. J. by STFC Ernest Rutherford Fellowship ST/L004399/1. Calibrated data from the Cassini mission are available from the NASA Planetary Data System at the Jet Propulsion Laboratory (https://pds.jpl.nasa.gov/).

References

Andrews, D. J., Coates, A. J., Cowley, S. W. H., Dougherty, M. K., Lamy, L., Provan, G., & Zarka, P. (2010). Magnetospheric period oscillations at Saturn: Comparison of equatorial and high-latitude magnetic field periods with north and south SKR periods. *Journal of Geophysical Research*, *115*, A12252. https://doi.org/10.1029/2010JA015666

Andrews, D. J., Cowley, S. W. H., Dougherty, M. K., Lamy, L., Provan, G., & Southwood, D. J. (2012). Planetary period oscillations in Saturn's magnetosphere: Evolution of magnetic oscillation properties from southern summer to post-equinox. *Journal of Geophysical Research*, *117*, A04224. https://doi.org/10.1029/2011JA017444

Arridge, C. S., André, N., Khurana, K. K., Russell, C. T., Cowley, S. W. H., Provan, G., et al. (2011). Periodic motion of Saturn's nightside plasma sheet. *Journal of Geophysical Research*, *116*, A11205. https://doi.org/10.1029/2011JA016827

Arridge, C. S., Khurana, K. K., Russell, C. T., Southwood, D. J., Achilleos, N., Dougherty, M. K., et al. (2008). Warping of Saturn's magnetospheric and magnetotail current sheets. *Journal of Geophysical Research*, *113*, A08217. https://doi.org/10.1029/2007JA012963

Badman, S. V., Bunce, E. J., Clarke, J. T., Cowley, S. W. H., Gérard, J.-C., Grodent, D., & Milan, S. E. (2005). Open flux estimates in Saturn's magnetosphere during the January 2004 Cassini-HST campaign, and implications for reconnection rates. *Journal of Geophysical Research*, *110*, A11216. https://doi.org/10.1029/2005JA011240

Badman, S. V., & Cowley, S. W. H. (2007). Significance of Dungey cycle flows in Jupiter's and Saturn's magnetospheres, and their identification on closed equatorial field lines. *Annales Geophysicae*, *25*, 941–951.

Badman, S. V., Cowley, S. W. H., Cecconi, B., Lamy, L., & Zarka, P. (2008). Relationship between solar wind corotating interaction regions and the phasing and intensity of Saturn kilometric radiation bursts. *Annales Geophysicae*, *26*, 3641–3651.

Badman, S. V., Masters, A., Hasegawa, H., Fujimoto, M., Radioti, A., Grodent, D., et al. (2013). Bursty magnetic reconnection at Saturn's magnetopause. *Geophysical Research Letters*, *40*, 1027–1031. https://doi.org/10.1002/grl.50199

Badman, S. V., Provan, G., Bunce, E. J., Mitchell, D. G., Melin, H., Cowley, S. W. H., et al. (2016). Saturn's auroral morphology and field-aligned currents during a solar wind compression. *Icarus*, *263*, 83–93. https://doi.org/10.1016/j.icarus.2014.11.014

Bunce, E. J., Cowley, S. W. H., Jackman, C. M., Clarke, J. T., Crary, F. J., & Dougherty, M. K. (2006). Cassini observations of the interplanetary medium upstream of Saturn and their relation to Hubble Space Telescope auroral data. *Advances in Space Research*, *38*, 806–814. https://doi.org/10.1016/j.asr.2005.08.005

Bunce, E. J., Cowley, S. W. H., Talboys, D. L., Dougherty, M. K., Lamy, L., Kurth, W. S., et al. (2010). Extraordinary field-aligned current signatures in Saturn's high-latitude magnetosphere: Analysis of Cassini data during Revolution 89. *Journal of Geophysical Research*, *115*, A10238. https://doi.org/10.1029/2010JA015612

Bunce, E. J., Cowley, S. W. H., Wright, D. M., Coates, A. J., Dougherty, M. K., Krupp, N., et al. (2005). In situ observations of a solar wind compression-induced hot plasma injection in Saturn's tail. *Geophysical Research Letters*, *32*, L20S04. https://doi.org/10.1029/2005GL022888

Carbary, J. F., & Mitchell, D. G. (2013). Periodicities in Saturn's magnetosphere. *Reviews of Geophysics*, *51*, 1–30. https://doi.org/10.1002/rog.20006

Carbary, J. F., Mitchell, D. G., Brandt, P., Roelof, E. C., & Krimigis, S. M. (2008). Periodic tilting of Saturn's plasma sheet. *Geophysical Research Letters*, *35*, L24101. https://doi.org/10.1029/2008GL036339

Chen, Y., Hill, T. W., Rymer, A. M., & Wilson, R. J. (2010). Rate of radial transport of plasma in Saturn's inner magnetosphere. *Journal of Geophysical Research*, *115*, A10211. https://doi.org/10.1029/2010JA015412

Clarke, J. T., Gérard, J.-C., Grodent, D., Wannawichian, S., Gustin, J., Connerney, J., et al. (2005). Morphological differences between Saturn's ultraviolet aurorae and those of Earth and Jupiter. *Nature*, *433*, 717–719.

Clarke, J. T., Nichols, J. D., Gérard, J.-C., Grodent, D., Hansen, K. C., Kurth, W. S., et al. (2009). The response of Jupiter's and Saturn's auroral activity to the solar wind. *Journal of Geophysical Research*, *114*, A05210. https://doi.org/10.1029/2008JA013694

Clarke, K. E., Andrews, D. J., Arridge, C. S., Coates, A. J., & Cowley, S. W. H. (2010). Magnetopause oscillations near the planetary period at Saturn: Occurrence, phase, and amplitude. *Journal of Geophysical Research*, *115*, A08209. https://doi.org/10.1029/2009JA014745

Clarke, K. E., Andrews, D. J., Coates, A. J., Cowley, S. W. H., & Masters, A. (2010). Magnetospheric period oscillations of Saturn's bow shock. *Journal of Geophysical Research*, *115*, A05202. https://doi.org/10.1029/2009JA015164

Cowley, S. W. H., Badman, S. V., Bunce, E. J., Clarke, J. T., Gérard, J.-C., Grodent, D., et al. (2005). Reconnection in a rotation-dominated magnetosphere and its relation to Saturn's auroral dynamics. *Journal of Geophysical Research*, *110*, A02201. https://doi.org/10.1029/2004JA010796

Cowley, S. W. H., & Bunce, E. J. (2003). Corotation-driven magnetosphere-ionosphere coupling currents in Saturn's magnetosphere and their relation to the auroras. *Annales Geophysicae*, *21*, 1691–1707.

Cowley, S. W. H., Bunce, E. J., & Prangé, R. (2004). Saturn's polar ionospheric flows and their relation to the main auroral oval. *Annales Geophysicae*, *22*, 1379–1394.

Cowley, S. W. H., Nichols, J. D., & Jackman, C. M. (2015). Down-tail mass loss by plasmoids in Jupiter's and Saturn's magnetospheres. *Journal of Geophysical Research: Space Physics*, *120*, 6347–6356. https://doi.org/10.1002/2015JA021500

Cowley, S. W. H., & Provan, G. (2017). Planetary period modulations of Saturn's magnetotail current sheet during northern spring: Observations and modeling. *Journal of Geophysical Research: Space Physics*, *122*, 6049–6077. https://doi.org/10.1002/2017JA023993

Cowley, S. W. H., Provan, G., Hunt, G. J., & Jackman, C. M. (2017). Planetary period modulations of Saturn's magnetotail current sheet: A simple illustrative mathematical model. *Journal of Geophysical Research: Space Physics*, *122*, 258–279. https://doi.org/10.1002/2016JA023367

Desch, M. D. (1982). Evidence for solar wind control of Saturn's radio emission. *Journal of Geophysical Research*, *87*, 4549–4554.
Desch, M. D., & Rucker, H. O. (1983). The relationship between Saturn kilometric radiation and the solar wind. *Journal of Geophysical Research*, *88*, 8999–9006. https://doi.org/10.1029/JA088iA11p08999
Dungey, J. W. (1961). Interplanetary field and the auroral zones. *Physical Review Letters*, *6*, 47–48.
Espinosa, S. A., Southwood, D. J., & Dougherty, M. K. (2003). How can Saturn impose its rotation period in a non-corotating magnetosphere? *Journal of Geophysical Research*, *108*(A2), 1086. https://doi.org/10.1029/2001JA005084
Grodent, D., Gérard, J.-C., Cowley, S. W. H., Bunce, E. J., & Clarke, J. T. (2005). Variable morphology of Saturn's southern ultraviolet aurora. *Journal of Geophysical Research*, *110*, A07215. https://doi.org/10.1029/2004JA010983
Grodent, D., Gustin, J., Gérard, J.-C., Radioti, A., Bonfond, B., & Pryor, W. R. (2011). Small-scale structures in Saturn's ultraviolet aurora. *Journal of Geophysical Research*, *116*, A09225. https://doi.org/10.1029/2011JA016818
Gurnett, D. A., Lecacheux, A., Kurth, W. S., Persoon, A. M., Groene, J. B., Lamy, L., et al. (2009). Discovery of a north-south asymmetry in Saturn's radio rotation period. *Geophysical Research Letters*, *36*, L16102. https://doi.org/10.1029/2009GL039621
Hill, T. W., Thomsen, M. F., Henderson, M. G., Tokar, R. L., Coates, A. J., McAndrews, H. J., et al. (2008). Plasmoids in Saturn's magnetotail. *Journal of Geophysical Research*, *113*, A01214. https://doi.org/10.1029/2007JA012626
Hunt, G. J., Cowley, S. W. H., Provan, G., Bunce, E. J., Alexeev, I. I., Belenkaya, E. S., et al. (2014). Field-aligned currents in Saturn's southern nightside magnetosphere: Sub-corotation and planetary period oscillation components. *Journal of Geophysical Research: Space Physics*, *119*, 9847–9899. https://doi.org/10.1002/2014JA020506
Jackman, C. J., Arridge, C. S., Krupp, N., Bunce, E. J., Mitchell, D. G., McAndrews, H. J., et al. (2008). A multi-instrument view of tail reconnection at Saturn. *Journal of Geophysical Research*, *113*, A11213. https://doi.org/10.1029/2008JA013592
Jackman, C. J., Lamy, L., Freeman, M. P., Zarka, P., Cecconi, B., Kurth, W. S., et al. (2009). On the character and distribution of lower-frequency radio emissions at Saturn and their relationship to substorm-like events. *Journal of Geophysical Research*, *114*, A08211. https://doi.org/10.1029/2008JA013997
Jackman, C. J., Russell, C. T., Southwood, D. J., Arridge, C. S., Achilleos, N., & Dougherty, M. K. (2007). Strong rapid dipolarizations in Saturn's magnetotail: In situ evidence of reconnection. *Geophysical Research Letters*, *34*, L11203. https://doi.org/10.1029/2007GL029764
Jackman, C. J., Slavin, J. A., & Cowley, S. W. H. (2011). Cassini observations of plasmoid structure and dynamics: Implications for the role of magnetic reconnection in magnetospheric circulation at Saturn. *Journal of Geophysical Research*, *116*, A10212. https://doi.org/10.1029/2011JA016682
Jackman, C. J., Slavin, J. A., Kivelson, M. G., Southwood, D. J., Achilleos, N., Thomsen, M. F., et al. (2014). Saturn's dynamic magnetotail: A comprehensive magnetic field and plasma survey of plasmoids and traveling compression regions and their role in global magnetospheric dynamics. *Journal of Geophysical Research: Space Physics*, *119*, 5465–5494. https://doi.org/10.1002/2013JA019388
Jackman, C. J., Thomsen, M. F., Mitchell, D. G., Sergis, N., Arridge, C. S., Felici, M., et al. (2015). Field dipolarization in Saturn's magnetotail with planetward ion flows and energetic particle flow bursts: Evidence of quasi-steady reconnection. *Journal of Geophysical Research: Space Physics*, *120*, 3603–3617. https://doi.org/10.1002/2015JA020995
Jackman, C. M., Achilleos, N., Bunce, E. J., Cecconi, B., Clarke, J. T., Cowley, S. W. H., et al. (2005). Interplanetary conditions and magnetospheric dynamics during the Cassini orbit insertion fly-through of Saturn's magnetosphere. *Journal of Geophysical Research*, *110*, A10212. https://doi.org/10.1029/2005JA011054
Jackman, C. M., Achilleos, N., Cowley, S. W. H., Bunce, E. J., Radioti, A., Grodent, D., et al. (2013). Auroral counterpart of magnetic field dipolarizations in Saturn's tail. *Planetary and Space Science*, *82*, 34–42.
Jackman, C. M., Provan, G., & Cowley, S. W. H. (2016). Reconnection events in Saturn's magnetotail: Dependence of plasmoid occurrence on planetary period oscillation phase. *Journal of Geophysical Research: Space Physics*, *121*, 2922–2934. https://doi.org/10.1002/2015JA021985
Jia, X., Kivelson, M. G., & Gombosi, T. I. (2012). Driving Saturn's magnetospheric periodicities from the upper atmosphere/ionosphere. *Journal of Geophysical Research*, *117*, A04215. https://doi.org/10.1029/2011JA017367
Krimigis, S. M., Sergis, N., Mitchell, D. G., Hamilton, D. C., & Krupp, N. (2007). A dynamic, rotating ring current around Saturn. *Nature*, *450*, 1050–1053.
Kurth, W. S., Gurnett, D. A., Clarke, J. T., Zarka, P., Desch, M. D., Kaiser, M. L., et al. (2005). An Earth-like correspondence between Saturn's auroral features and radio emissions. *Nature*, *433*, 722–725.
Lamy, L., Cecconi, B., Zarka, P., Canu, P., Schippers, P., Kurth, W. S., et al. (2011). Emission and propagation of Saturn kilometric radiation: Magnetoionic modes, beaming pattern, and polarization state. *Journal of Geophysical Research*, *116*, A04212. https://doi.org/10.1029/2010JA016195
Lamy, L., Prangé, R., Pryor, W., Gustin, J., Badman, S. V., Melin, H., et al. (2013). Multispectral diagnosis of Saturn's aurorae throughout a planetary rotation. *Journal of Geophysical Research: Space Physics*, *118*, 4817–4843. https://doi.org/10.1002/jgra.50404
Lamy, L., Schippers, P., Zarka, P., Cecconi, B., Arridge, C. S., Dougherty, M. K., et al. (2010). Properties of Saturn kilometric radiation measured within its source region. *Geophysical Research Letters*, *37*, L12104. https://doi.org/10.1029/2010GL043415
Liu, X., & Hill, T. W. (2012). Effects of finite pressure on centrifugally driven convection in Saturn's inner magnetosphere. *Journal of Geophysical Research*, *117*, A07216. https://doi.org/10.1029/2012JA017827
Liu, X., Hill, T. W., Wolf, R. A., Sazykin, S., Spiro, R. W., & Wu, H. (2010). Numerical simulation of plasma transport in Saturn's inner magnetosphere using the Rice Convection Model. *Journal of Geophysical Research*, *115*, A12254. https://doi.org/10.1029/2010JA015859
Mardia, K. V., & Jupp, P. E. (2000). *Directional Statistics*. Chichester, UK: J. Wiley and Sons Ltd.
McPherron, R. L., Russell, C. T., & Aubrey, M. P. (1973). Satellite studies of magnetospheric substorms on August 15, 1968, 9, Phenomenological model for substorms. *Journal of Geophysical Research*, *78*, 3131–3149. https://doi.org/10.1029/JA078i016p03131
Meredith, C. J., Cowley, S. W. H., & Nichols, J. D. (2014). Survey of Saturn auroral storms observed by the Hubble Space Telescope: Implications for storm time scales. *Journal of Geophysical Research: Space Physics*, *119*, 9624–9642. https://doi.org/10.1002/2014JA0020601
Milan, S. E., Hutchinson, J., Boakes, P. D., & Hubert, B. (2009). Influences on the radius of the auroral oval. *Annales Geophysicae*, *27*, 2913–2924.
Mitchell, D. G., Brandt, P. C., Roelof, E. C., Dandouras, J., Krimigis, S. M., Mauk, B. H., et al. (2005). Energetic ion acceleration in Saturn's magnetotail: Substorms at Saturn? *Geophysical Research Letters*, *32*, L20S01. https://doi.org/10.1029/2005GL022647
Mitchell, D. G., Krimigis, S. M., Paranicas, C. P., Brandt, P. C., Carbary, J. F., Roelof, E. C., et al. (2009). Recurrent energization of plasma in the midnight-to-dawn quadrant of Saturn's magnetosphere, and its relationship ion to auroral UV and radio. *Planetary and Space Science*, *57*, 1732–1742. https://doi.org/10.1016/j.pss.2009.04.002
Morooka, M. W., Modolo, R., Wahlund, J.-E., André, M., Eriksson, A. I., Persoon, A. M., et al. (2009). The electron density of Saturn's magnetosphere. *Annales Geophysicae*, *27*, 2971–2991.
Nichols, J. D., Badman, S. V., Baines, K. H., Brown, R. H., Bunce, E. J., Clarke, J. T., et al. (2014). Dynamic auroral storms on Saturn as observed by the Hubble Space Telescope. *Geophysical Research Letters*, *41*, 3323–3330. https://doi.org/10.1002/2014GL060186

Pilkington, N. M., Achilleos, N., Arridge, C. S., Guio, P., Masters, A., Ray, L. C., et al. (2015). Internally driven large-scale changes in the size of Saturn's magnetosphere. *Journal of Geophysical Research: Space Physics*, *120*, 7289–7306. https://doi.org/10.1002/2015JA021290

Pontius, D. H. Jr., & Hill, T. W. (2009). Plasma mass loading from the extended neutral gas torus of Enceladus as inferred from the observed plasma corotation lag. *Geophysical Research Letters*, *36*, L23013. https://doi.org/10.1029/2009GL041030

Prangé, R., Pallier, L., Hansen, K. C., Howard, R., Vourladis, A., Courtin, R., & Parkinson, C. (2004). An interplanetary shock traced by planetary auroral storms from the Sun to Saturn. *Nature*, *432*, 78–81. https://doi.org/10.1038/nature02986

Provan, G., Andrews, D. J., Arridge, C. S., Coates, A. J., Cowley, S. W. H., Cox, G., et al. (2012). Dual periodicities in planetary-period magnetic field oscillations in Saturn's tail. *Journal of Geophysical Research*, *117*, A01209. https://doi.org/10.1029/2011JA017104

Provan, G., Cowley, S. W. H., Lamy, L., Bunce, E. J., Hunt, G. J., Zarka, P., & Dougherty, M. K. (2016). Planetary period oscillations in Saturn's magnetosphere: Coalescence and Reversal of northern and southern periods in late northern spring. *Journal of Geophysical Research: Space Physics*, *121*, 9829–9862. https://doi.org/10.1002/2016JA023056

Provan, G., Cowley, S. W. H., Sandhu, J., Andrews, D. J., & Dougherty, M. K. (2013). Planetary period magnetic field oscillations in Saturn's magnetosphere: Post-equinox abrupt non-monotonic transitions to northern system dominance. *Journal of Geophysical Research: Space Physics*, *118*, 3243–3264. https://doi.org/10.1002/JGRA.50186

Radioti, A., Grodent, D., Gérard, J.-C., Bonfond, B., Gustin, J., Pryor, W., et al. (2013). Auroral signatures of multiple magnetopause reconnection at Saturn. *Geophysical Research Letters*, *40*, 4498–4502. https://doi.org/10.1002/grl.50889

Radioti, A., Grodent, D., Gérard, J.-C., Milan, S. E., Bonfond, B., Gustin, J., & Pryor, W. (2011). Bifurcations of the main auroral ring at Saturn: Ionospheric signatures of consecutive reconnection events at the magnetopause. *Journal of Geophysical Research*, *116*, A11209. https://doi.org/10.1029/2011JA016661

Radioti, A., Grodent, D., Jia, X., Gérard, J.-C., Bonfond, B., Pryor, W., et al. (2016). A multi-scale magnetotail reconnection event at Saturn and associated flows: Cassini/UVIS observations. *Icarus*, *263*, 75–82. https://doi.org/10.1016/j.icarus.2014.12.016

Reed, J. J., Jackman, C. M., Lamy, L., Kurth, W. S., & Whiter, D. K. (2018). Low-frequency extensions of the Saturn kilometric radiation as a proxy for magnetospheric dynamics. *Journal of Geophysical Research: Space Physics*, *123*, 443–463. https://doi.org/10.1002/2017JA024499

Slavin, J. A., Smith, M. F., Mazur, E. L., Baker, D. N., Hones, E. W., Iyemori, T., & Greenstadt, E. W. (1993). ISEE 3 observations of traveling compression regions in the Earth's magnetotail. *Journal of Geophysical Research*, *98*(A9), 15,425–15,446.

Smith, A. W., Jackman, C. M., & Thomsen, M. F. (2016). Magnetic reconnection in Saturn's magnetotail: A comprehensive magnetic field survey. *Journal of Geophysical Research: Space Physics*, *121*, 2984–3005. https://doi.org/10.1002/2015JA022005

Smith, A. W., Jackman, C. M., Thomsen, M. F., Lamy, L., & Sergis, N. (2018). Multi-instrument investigation of the location of Saturn's magnetotail x-line. *Journal of Geophysical Research: Space Physics*, *123*, 5494–5505. https://doi.org/10.1029/2018JA025532

Smith, A. W., Jackman, C. M., Thomsen, M. F., Sergis, N., Mitchell, D. G., & Roussos, E. (2018). Dipolarization fronts with associated energized electrons in Saturn's magnetotail. *Journal of Geophysical Research: Space Physics*, *123*, 2714–2735. https://doi.org/10.1002/2017JA024904

Szego, K., Nemeth, Z., Foldy, L., Cowley, S. W. H., & Provan, G. (2013). Dual periodicities in the flapping of Saturn's magnetodisk. *Journal of Geophysical Research: Space Physics*, *118*, 2883–2887. https://doi.org/10.1002/jgra.50316

Thomsen, M. F., Jackman, C. M., Cowley, S. W. H., Jia, X., Kivelson, M. G., & Provan, G. (2017). Evidence for periodic variations in the thickness of Saturn's nightside plasma sheet. *Journal of Geophysical Research: Space Physics*, *122*, 280–292. https://doi.org/10.1029/2016JA023368

Thomsen, M. F., Jackman, C. M., Mitchell, D. G., Hospodarsky, G., Kurth, W. S., & Hansen, K. C. (2015). Sustained lobe reconnection in Saturn's magnetotail. *Journal of Geophysical Research: Space Physics*, *120*, 10,257–10,274. https://doi.org/10.1002/2015JA021768

Thomsen, M. F., Wilson, R. J., Tokar, R. L., Reisenfeld, D. B., & Jackman, C. M. (2013). Cassini/CAPS observations of duskside tail dynamics at Saturn. *Journal of Geophysical Research: Space Physics*, *118*, 5767–5781. https://doi.org/10.1002/jgra.50552

Vasyliunas, V. M. (1983). In A. J. Dessler (Ed.), *Plasma distribution and flow. Physics of the Jovian magnetosphere* (pp. 395–453). New York: Cambridge University Press.